



Preface and Acknowledgement

This thesis is written as a part of the first stage of the project SOILSPACE “Quantifying Soil Structure to Augment the Relevance of Laboratory-Based Soil Hydraulic Properties for Environmental Modelling” funded by the Norwegian Research council (240663/F20). As part of the project, researchers from different institutions collaborate on improving the characterization of soil hydrological processes through pedotransfer functions (PTFs).

I would first and foremost like to thank my supervisor Helen Kristine French (NMBU) for all her help throughout this year and for always having an open door. The helpful advice, constructive feedback, and moral support are all greatly appreciated. I would also like to thank the researchers that are working on the SOILSPACE project, especially Attila Nemes, Esther Bloem, Annette Dathe (Nibio), and Matthew Patterson (Rutgers Uni.) for welcoming me on your project.

Furthermore, I would like to thank Magdalena Rygalska, Trond Børresen, and Øyvind Peder Vartdal (NMBU) for all of your laboratory assistance. I would also like to thank Leif Vidar Jacobsen (NMBU) for giving me an introduction on usage of the equipment, both in the field and later in the laboratory. Thank you to NGI for lending me equipment and especially thanks to Thomas Pabst for arranging it and for giving me an introduction on operational practices.

Additionally, a special thanks goes out to Eirik Magnus Bache Stokmo for assisting me in the field. Your presence not only made the fieldwork more efficient, but also a lot more enjoyable.

Finally, I would like to thank Mari Katrine Tvedten for proofreading and my family and friends for encouraging words and moral support.

Andrea Nymo Fikse

Ås, 13.05.2016

Abstract

A number of different soil physical properties, including the size, form, and distribution of pores in the soil matrix, affects water movement in the unsaturated zone and, consequently, its ability to deal with various amounts of precipitation. Knowledge regarding the extent and structure of variability of the properties are important for predicting the outcome of the variations that might exist. Despite the high importance of the physical properties, their quantification is a rear prioritization due to their high cost. The solution might be to use pedotransfer functions (PTFs) as they provide a pragmatic alternative to direct measurements of physical properties. PTFs are implemented to predict physical properties from parameters collected during soil surveys.

The main objective of this thesis is to characterize the spatial variability of the physical properties that might exist on cultivated land. Through the implementation of different methods, including electrical resistivity tomography (ERT), double-ring infiltration tests, and water retention characteristics and grain size distribution analyses, a field plot southeast in the Skuterud catchment has been studied with the intention of characterizing the spatial variability in the topsoil, examining spatiotemporal variability, and simulating changes in unsaturated flow with varying precipitation patterns and amounts. As compaction is a stressing concern in conventional agriculture, mainly due to vehicular activity, the effect that topsoil and subsoil compaction might have on the flow through the soil matrix has been studied in the graphical computer platform HYDRUS using the van Genuchten parameterization of the water retention curve.

Two vertical cross-sections have been created in HYDRUS, where the designs are based on findings through soil exploratory methods. They were implemented to simulate the effect of topsoil and subsoil compaction in combination with different patterns and amounts of precipitation on the vertical movement of water in the unsaturated zone. Based on these findings, it is evident that compaction of the soil decreases the rate of flow through the soil matrix, especially during unsaturated conditions. Though verification of the two models is still required, the double-ring infiltration tests and the geostatistical analyses of the soil

physical parameters support these findings as they imply how compacted areas have decreased hydraulic conductivities and, hence, rate of flow.

To indirectly explore the vertical spatiotemporal variability of the soil, time-lapse ERT surveys have been conducted from December 2015 to April 2016. The ERT was implemented to investigate the temporal change of resistivity values in the soil matrix during a period of snowmelt and induced infiltration. Though the resistivity values were generally expected to decrease between the measurements, the resulting images portrayed increasing values. Measurements of soil temperatures reveal that there had been a slight decrease in the temperature between a few of the measurements, which could possibly lead to increasing resistivity values due to increasing fluid viscosity. A plausible theory as to why the resistivity values continued to increase during a period of induced snowmelt might include preferential flow ways through macro-pores that generated large amounts of water rapidly, which resulted in low water contents by the time of the ERT measurements. Further analyses are needed to support this theory or to propose an alternate advocate suggestion.

Table of Contents

Preface and Acknowledgement.....	i
Abstract.....	iii
List of Figures.....	ix
List of Tables.....	xii
1 Introduction.....	1
1.1 SOILSPACE.....	2
1.2 Objectives.....	3
2 Area Description.....	5
2.1 The Skuterud catchment	5
2.2 Climate.....	5
2.3 Geology and hydrogeology of the area	6
2.4 Choice of field area	7
3 Theory.....	9
3.1 Unsaturated flow	9
3.1.1 Soil Structure	9
3.1.2 Flow in the unsaturated zone	10
3.1.3 Infiltration in the unsaturated zone.....	14
3.2 Soil compaction	14
3.2.1 Compaction in theory	14
3.2.2 Compaction in agriculture.....	15
3.3 Electrical resistivity	15
3.3.1 Basic principles	15
3.3.2 In the field.....	17
3.4 Computer modelling and analysis	18
3.4.1 Geostatistical analysis with SGeMS	18
3.4.2 Simulation of water flow with HYDRUS	19
4 Methods.....	21
4.1 Electrical resistivity tomography	21
4.2 Dielectric water potential sensor and TDR sensor.....	22
4.3 Double-ring infiltration test	24

4.4	Sounding	25
4.5	Sediment sampling	26
4.6	Sediment sample analysis	27
4.6.1	Grain size distribution.....	27
4.6.2	Water retention characteristics.....	29
4.7	Computer modelling	32
4.7.1	SGeMS.....	32
4.7.2	HYDRUS.....	32
5	Results	37
5.1	Electrical resistivity tomography	37
5.1.1	Absolute resistivity images.....	38
5.1.2	Temporal changes in resistivity.....	40
5.2	Infiltration	41
5.3	Grain size distribution analysis	42
5.4	Water retention characteristics	43
5.5	SGeMS	46
5.5.1	Grain size distribution.....	49
5.5.2	Water retention characteristics.....	50
5.5.3	In-situ water retention parameters.....	54
5.6	HYDRUS	57
5.6.1	Simulations of flow and the impact of compaction.....	57
5.6.2	Changes in velocity.....	59
5.6.3	Drainage efficiency.....	61
5.6.4	Dispersion of tracer plumes.....	61
6	Discussion	63
6.1	Physical measurements	63
6.1.1	Temporal changes in resistivity.....	63
6.1.2	Determining the existence of compaction.....	65
6.2	Simulations	67
6.2.1	Topsoil and subsoil compaction and its influence on drainage efficiency.....	68
6.3	The positive sides of compaction	69
6.4	Preventative actions against compaction	69
7	Conclusion	71
8	Bibliography	75

Appendix.....	i
Appendix A.....	ii
Appendix B.....	iii
Appendix C.....	iv
Appendix D.....	ix

List of Figures

Figure 2-1: The dispersion of land use and soil types in the Skuterud catchment (Kalantari et al. 2015).	6
Figure 2-2: A dug trench portraying a 1 m deep soil profile. The plough layer stands out from the other layers by its dark brown colour. Photo: Andrea Nymo Fikse.	7
Figure 2-3: Map of the field area its location in Ås, Norway. Created in Google Earth.	8
Figure 2-4: Tile drains have been implemented in different directions in the Skuterud catchment. The field area relative to the direction of the drains is portrayed here. The field plot is not to scale (Stolte 2016).	8
Figure 3-1: Suction plotted against the volumetric water content in a water retention curve (Schwartz and Zhang 2003).	12
Figure 3-2: A sketch of the simple definition of resistivity across a cube with side length (L) with an applied current (I) and the potential drop between opposite sides (V) (adapted from Reynolds (2011)).	16
Figure 4-1: The layout of the ERT lines, in meters. Each red dot represents an electrode. Created with Adobe Illustrator.	21
Figure 4-2: Image (A) shows how the ERT cable had to be laid out for the electrodes to have a spacing of 0.5 meters and (B) shows an electrode and how it is connected to the cable. Photo: Andrea Nymo Fikse.	22
Figure 4-3: Moisture content and suction was measured every two meters in each direction, as well as every 20 centimetres in two squares as portrayed in the image. The data from the two smaller squares was to be used in calculating spatial variability. Created with Adobe Illustrator.	23
Figure 4-4: The TDR sensor and the dielectric water potential sensor (A) connect to data loggers (B). They were pushed into the ground approximately five centimetres apart (C). Photo: Andrea Nymo Fikse.	24
Figure 4-5: Six double-ring infiltration tests were performed, where three of them were on tire tracks, while the remaining three were between tire tracks. Created with Adobe Illustrator.	25
Figure 4-6: The researched field plot in meters, including the locations for the soil samples. Two sediment samples were collected every three meters in each direction. In the	

two smaller plots, only one sample was collected form each location to be used towards spatial variability. Created with Adobe Illustrator.....	26
Figure 4-7: The steel cylinder had to be completely filled with soil, as shown in (A). To achieve this, a hammering head, as is shown in (B), was put on top of the ring before applying a hammer to beat the ring into the ground. Photo: Andrea Nymo Fikse.....	27
Figure 5-1: The changes in temperature in °C and the incoming precipitation in millimetres from 03/12/2015 to 01/04/2016. Included on the temperature graph are labels named “ERT” to point out when the measurements where taken relative to the climatic situation.....	37
Figure 5-2: The resulting ERT images from the time-lapse measurements with results from 03/12/2015, 14/01/2016, 26/01/2016, 29/01/2016, 12/02/2016, and 01/04/2016. The colour codes of the resistivity values are displayed with the colour scale, which is given in Ωm . The stippled lines show positions of tire tracks.....	39
Figure 5-3: Percentage change in resistivity values from the previous measurement. Hence, 14/01/2016 shows the percentage change from 03/12/2015, 26/01/2016 from 14/01/2016, and so on. The stippled lines indicate positions of tire tracks.	40
Figure 5-4: A modified version of the USDA (1993) soil triangle that includes the results from the sediment samples analysed.	42
Figure 5-5: Water retention (pF) curves of the soil samples that were analysed for water retention characteristics portraying the volumetric water contents at different pF values.	44
Figure 5-6: The relationship between the hydraulic conductivity and the density of the soil samples. The red squares represent soil samples excavated from tire tracks, while the blue diamonds represent soil samples excavated between tracks.....	45
Figure 5-7: Omnidirectional variograms of clay (A), silt (B), and sand (C) from the grain size distribution analysis. Created in SGeMS.....	49
Figure 5-8: The kriged maps of clay (A), silt (B), and sand (C) from the grain size distribution analysis. The scales are given in %. Created in SGeMS.....	50
Figure 5-9: Omnidirectional variograms of air capacity (A), air permeability (B), density (C), hydraulic conductivity (D), porosity (E), residual volumetric water content (F), saturated volumetric water content (G), and the van Genuchten parameters α (H) and n (I) from the water retention characteristics analysis. Created in SGeMS.....	51

Figure 5-10: The kriged maps of air capacity in vol% (A), air permeability in μm^2 (B), density in g/cm^3 (C), hydraulic conductivity in m/day (D), porosity in vol% (E), residual volumetric water content in vol% (F), saturated volumetric water content in vol% (G), the van Genuchten parameter α in $1/\text{m}$ (H) and the dimensionless van Genuchten parameter n from the water retention characteristics analysis. Created in SGeMS..... 54

Figure 5-11: Omnidirectional variograms of suction (A), temperature (B), and volumetric water content (C) from the in-situ measurements of water retention parameters. Created in SGeMS. 55

Figure 5-12: The kriged maps of suction in kPa (A), temperature in $^{\circ}\text{C}$ (B), and volumetric water content in m^3/m^3 (C) from the in-situ measurements of water retention characteristics. Created in SGeMS. 56

Figure 5-13: Directional variograms of temperature portraying the range of correlation in the 0° and 45° angles. Created in SGeMS. 56

Figure 5-14: The cumulative precipitation during M1, M2, and M3 used to define the top boundary flux in the HYDRUS models..... 57

Figure 5-15: The breakthrough curves of the three scenarios M1, M2, and M3 extended to 60 days in the two models Cross-Section 1 and Cross-Section 2 (CS1 and CS2, respectively)..... 58

Figure 5-16: The colour scale and spreading of the tracer on M2:11, in Cross-Section 1 (A) and Cross-Section 2 (B). The cross-sections are both grey at the top as the concentration of the tracer is not within the scaling range. Created in HYDRUS 2.04. 59

Figure 5-17: The change of velocity on M1:5 in Cross-Section 1 is portrayed isolines and velocity vectors, where the vectors depict the direction of flow. The red arrows are included to accentuate this. The colour scale is also provided. Created in HYDRUS 2.04. 60

Figure 5-18: The change of velocity on M1:5 in Cross-Section 2 is portrayed with isolines and velocity vectors, where the vectors depict the direction of flow. The red arrows are included to accentuate this. The colour scale is also provided. Created in HYDRUS 2.04..... 60

Figure 5-19: The scale and the spreading of the three tracer plumes in Cross-Section 2, where A-F represent M3:2, M3:5, M3:12, M3:19, M3:23, and M3:31, respectively.

The grey areas represent where the concentration is higher than the given scale.
 Created in HYDRUS 2.04. 62

List of Tables

Table 5-1: The dates of measurement with the temperature of that specific day and the incoming precipitation of the previous seven days..... 38

Table 5-2: The coordinates for each of the tests, indication for whether they were on or off a tire track, and the calculated rate of infiltration..... 41

Table 5-3: Statistical analysis of the resulting hydraulic conductivities from the infiltration tests, including minimum and maximum values, mean, median, skew, standard deviation (σ), and variance (σ^2). 42

Table 5-4: Statistical analysis of the resulting distribution of grain sizes from the grain size distribution analysis, including minimum and maximum values, mean, median, skew, standard deviation (σ), and variance (σ^2) of clay, silt, and sand. 43

Table 5-5: Statistical analysis, including minimum and maximum values, mean, median, skew, standard deviation (σ), and variance (σ^2), of the parameters from the water retention characteristics hydraulic conductivity, saturated and residual water content, air capacity, density, and porosity and the in-situ measurements of the water retention parameters water content, suction, and temperature..... 44

Table 5-6: Statistical analysis of the parameters density and hydraulic conductivity from the tire tracks and between the tire tracks, including minimum and maximum values, mean, median, skew, standard deviation (σ), and variance (σ^2). 46

Table 5-7: The average values of soil density (ρ), porosity (n), and the hydraulic conductivities of compacted ($K_{s \text{ sub}}$) and uncompact (K_s) soil from the water retention characteristics analysis, as well as a van Genuchten parameter (n) produced by SWRC Fit with the results from the same analysis. 46

Table 5-8: The calculated correlations between the in-situ measured water retention parameters water content, suction, and temperature..... 47

Table 5-9: The calculated correlations between the grain sizes from the grain size distribution, clay, silt, and sand, and the parameters from the water retention characteristics analyses, hydraulic conductivity, saturated and residual water content, air capacity, density, porosity and the van Genuchten parameters n and α .48

List of Tables

Table 5-10: The retention time of the scenarios M1, M2, and M3 in both of the cross-sections and the precipitating water during this period of time.....	58
Table 5-11: The drainage efficiency of the tile drain in Cross-Section 1 and Cross-Section 2 during M1, M2, and M3.	61

1 Introduction

The soil physical properties of an area have a great impact on its ability to deal with numerous types of climatic variations. Knowledge of the extent and structure of variability of these properties affects the ability to predict how the soil might deal with different climatic conditions (Kværnø et al. 2007). In the northern part of the temperate climatic zone, the soil has to withstand seasonal change with a variety of climatic conditions. Especially in agriculture, it is vital to comprehend the hydrogeology of the soil to predict the outcome of the seasonal changes that follows. Kværnø et al. (2007) claim that even though the soil physical properties are important, the high costs make their quantification a rear prioritisation. This might be problematic as only a few soil variables can be derived from the optimal sources of information (i.e. the soil map and databases from soil surveys) and that the variability and uncertainty within map units is not included (Kværnø et al. 2007). In fact, a well-known issue when developing computer models to simulate water and solute movement in the unsaturated zone has been the lack of accurate hydraulic properties; especially water retention properties and hydraulic conductivity. As described by Wösten et al. (1999), the solution might be to use pedotransfer functions (PTFs), which are implemented to predict soil physical properties from parameters collected during soil surveys. The use of these functions is pragmatically the best option for costly and time-consuming direct measurements of physical properties.

In agriculture, information concerning variability of the soil physical properties is meaningful as it might impact the treatment of the soil and the resulting produce. It is indeed possible to improve model simulations by including soil variability information and increasing the resolution of soil data. By creating more realistic simulations, it might be plausible for farmers to adjust their cultivation practices based on the results. In conventional agriculture, one of the major problems is soil compaction and the extent of compacted soils from vehicular activity is estimated at 68 million ha of land globally (Hamza and Anderson 2005), where 33 million ha is in Europe (Flowers and Lal 1998). As there might not be any evident signs at the soil surface, it can be difficult to locate and rationalize. Causes of compaction include overuse of machinery, intensive cropping, short crop rotations, intensive grazing, and inappropriate soil management. In a controlled traffic system, for instance, the volumetric density and compaction might increase by 15-39% and 39-272% in the tire tracks

compared to the areas between the tracks, and the porosity might consequently decrease by 8% (Hamza and Anderson 2005). Compaction might occur both in the topsoil and the subsoil, with subsoil compaction being more severe than topsoil compaction. Subsoil compaction might influence the soil deep into the profile; according to Arvidsson (2001), traffic with 10 Mg axle load at an inflation pressure at approximately 300 kPa might increase compaction as deep as 50 cm below the surface on most soil types during wet conditions. The changes to the physical properties of the soil tend to be enduring, and might influence the production capacity of the soil for more than five years after the traffic was applied.

By increasing soil strength and decreasing soil physical fertility, as a result of a decreased storage and supply of water and nutrients, there is a higher demand for fertiliser and the production cost increases as a result. Hence, compaction is economically burdensome for farmers. Compaction of the soil as well as poor seedbed preparation might also lead to higher runoff and erosion risk (Kværnø et al. 2007). The modifications of soil properties might additionally increase the emission of greenhouse gases and the movement of nitrate and pesticides into the groundwater (Soane and Ouwerkerk 1995). If the variability of the soil is quantified and there is a distinct difference between the soil that has been compacted as a result of e.g. vehicular activity and the soil that has not, the farmer has the opportunity to transform his agricultural routine for increased workability of the soil.

1.1 SOILSPACE

This Master's thesis is part of the four-year-long project SOILSPACE "Quantifying Soil Structure to Augment the Relevance of Laboratory-Based Soil Hydraulic Properties for Environmental Modelling" funded by the Norwegian Research council (240663/F20). Researchers from NMBU, NIBIO, SLU and Rutgers University collaborate on improving the characterization of soil hydrological processes through pedotransfer functions (PTFs). The ultimate aim is to increase the efficiency of the establishment/reestablishment of environmental quality and ecosystem services. The researchers also intend to assist in improving the efficiency of agricultural and environmental planning and remediation studies (Nemes 2015). Two sites in Norway have been selected for the research project: the Skuterud catchment in Ås and the Gardermoen field site at Moreppen. This thesis focuses on the Skuterud site and is part of the first stage of the project, which includes the characterization of field effective hydraulic behaviour in space and time.

1.2 Objectives

The main objective is to characterize the spatial variability of the physical properties that might exist on cultivated land through different kinds of physical research methods, such as electrical resistivity tomography, double-ring infiltration tests, and water retention characteristics and grain size distribution analyses. Specific objectives within this thesis includes to

- characterize the spatial variability in the top soil
- observe how the resistivity varies with time across the grid
- simulate the results of periods of high/low precipitation and examine how the tilting of the models and the tile drains affects the resulting flow
- determine how compaction as a result of vehicular activity affects the infiltration capacity of the soil and discuss how that might have an impact on crop production.

2 Area Description

2.1 *The Skuterud catchment*

The Skuterud catchment, which is the catchment surrounding the Skuterud creek, is located in the Ås and Ski municipalities in Akershus county, approximately 30 km south of Oslo (see Figure 2-3). The catchment spans across a 4489 daa large area (Øygarden et al. 2010), where about 60% consists of cultivated land (mainly cereal, potato, and ley crop production)(Kalantari et al. 2015). Long and gentle slopes dominate the west side of the creek in the catchment area, while the east side has shorter and deeper inclines. The southeastern part of the field includes a 244 daa large residential neighbourhood. There are also forested areas along the edges of the catchment. The elevation in the catchment only has small variations by Norwegian standards, and it fluctuates between 91 and 146 masl (Greipsland et al. 2013).

The Skuterud catchment has served as part of the Environmental Agricultural Monitoring Program in Norway (JOVA) since 1993 (Kværnø et al. 2007, Bechmann et al. 2014). JOVA started in 1992 with the purpose of documenting the environmental effects of agricultural practices, as well as measuring runoff from the fields and water quality. Eleven catchment areas have been selected to be apart of the program; registration of the runoff and sampling for further analyses of nutrients and particles are done on a continuous basis. The specific agricultural fields were chosen as they represent the most important cultivated areas in Norway based on climate, soils, and operational practices (Hauken 2015).

2.2 *Climate*

The lowest mean monthly temperature measured in Ås is -4.8 °C in January/February, while the maximum is 16.1 °C in July. The mean annual temperature is 5.3 °C.

According to a report by JOVA from 2014, the mean temperature in Skuterud was 5.5 °C and the total amount of precipitation was 785 mm within the period of 2012-2013 (Bechmann et al. 2014). Unstable winters, with variable snow cover, and hot summers characterize the area, and its growing season, i.e. the number of days with a temperature above 5 °C (Mueller et al. 2015), is approximately 194 days a year (Sørbotten 2011).

2.3 *Geology and hydrogeology of the area*

The quaternary map produced by the Geological Survey of Norway (NGU) in Appendix A portrays that the area is largely composed of marine deposits and clay loam to silty clay loam (Figure 2-1). At one point, there was a shoreline in the Skuterud catchment as is evident by the thick beach deposit. Materials that are typical of shore areas (e.g. shells and charcoal) have been located in these deposits. In the quaternary map, it is also evident that an ice sheet has previously covered the area. Thick moraine material originating from Younger Dryas (12 ka ago) is found in marginal moraine ridges that traverse the Skuterud catchment (Kalantari et al. 2013).

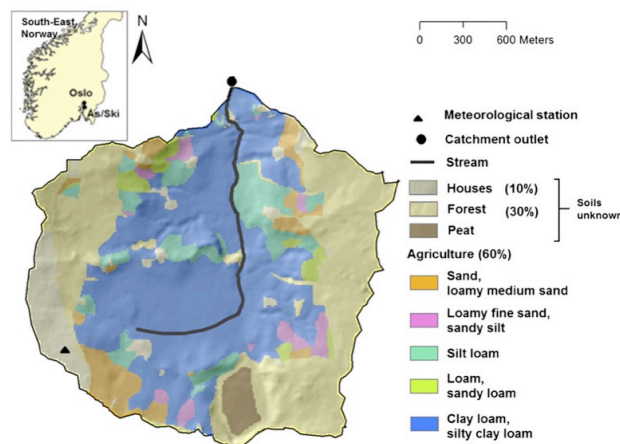


Figure 2-1: The dispersion of land use and soil types in the Skuterud catchment (Kalantari et al. 2015).

As 60% of the Skuterud catchment is cultivated land, the top layer of sediment is strongly affected by cultivation practices. As seen in the trench in Figure 2-2, the top layer, i.e. the plough layer, reaches 20-30 cm into the ground. Through inspections of the trench, it is indisputable that these sediments are mechanically mixed, while the mixing of the layers below occurs through bioturbation (i.e. mixing by organisms such as earth worms). Bioturbation channels were visible as many of them were filled with silt or clay (guided tour by Trond Haraldsen, 23/10/2015).



Figure 2-2: A dug trench portraying a 1 m deep soil profile. The plough layer stands out from the other layers by its dark brown colour. Photo: Andrea Nymo Fikse.

A sounding test in the plot demonstrated how homogeneous the sediments are from the surface and down to approximately 9.5 meters. From that point and down, the grain size increased and the crunching sound that appeared can possibly indicate till from a basal moraine. The bedrock was reached at a depth of 10.5 meters.

2.4 Choice of field area

Several criteria affected the decision of choice of field plot. First, it was essential to choose an area that was relatively flat to have as little surface runoff as possible. If runoff were occurring, it would be necessary to monitor it to get the right water balance. Surface runoff might additionally cause erosion of the surface and thereby change the characteristics of the area, especially over a period of several years. It was also important to choose the plot in an area with homogeneous clayey soil. The field area chosen for this project is located southeast in the Skuterud catchment on an agricultural field. Additional measurements were conducted in a smaller part of the selected field area as part of the SOILSPACE project, including temporal measurements of suction and volumetric water content at different depths and CT scanning of undisturbed soil samples for detailed 3D views of the size, form, and distribution of pores.

Area Description

In the chosen area, an 11.5m x 23.5m rectangle was marked. This smaller area is where the research for this thesis was conducted, as illustrated in Figure 2-3.



Figure 2-3: Map of the field area its location in Ås, Norway. Created in Google Earth.

In the Skuterud catchment, tile drains have been implemented at 0.8 meters depth. Figure 2-4 portrays a rough sketch of the direction of these drains in the part of the catchment where the plot is situated. The chosen field plot is included to illustrate how it is placed relative to the drains. Excavation of trenches also revealed that an old drainage system exists at approximately 1 meters depth.

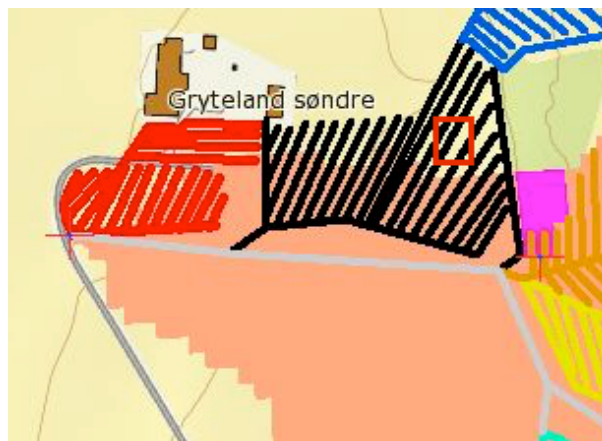


Figure 2-4: Tile drains have been implemented in different directions in the Skuterud catchment. The field area relative to the direction of the drains is portrayed here. The field plot is not to scale (Stolte 2016).

3 Theory

3.1 *Unsaturated flow*

This thesis focuses on the unsaturated part of the hydrogeological system, the unsaturated zone.

3.1.1 Soil Structure

The unsaturated zone is the part of the ground in which the soil pores are not fully saturated with liquid. Except for the capillary fringe, i.e. the area directly above the groundwater table that is saturated due to the capillary forces, the pores in this zone contain both liquid and gases. The porosity, i.e. the percentage of the rock that is void space, is therefore fundamental as it influences the amount of liquid required to saturate the ground. When considering porosity, it is important to distinguish between *total porosity* and *effective porosity* (Domenico and Schwartz 1998). Total porosity is a measure of all the pores in the soil and it does not require pore connections, while effective porosity only considers the pores that are connected to one another as they are the ones in which liquid will pass through. Effective porosity can be calculated by

$$n_e = \frac{V_v}{V_T} \quad \text{Equation 1}$$

where n_e is the effective porosity, V_v is the volume of the interconnected pores (m^3), and V_T is the total volume (m^3). How much liquid the pores contain is represented by the *volumetric water content*, θ , which can be calculated by

$$\theta = \frac{V_w}{V_T} \quad \text{Equation 2}$$

where V_w is the volume of water (m^3) and V_T is the volume of soil (m^3). While the volumetric water content describes how much water the soil contains compared to how much soil there is, the *water saturation*, S , describes the degree of saturation. It is defined as

$$S = \frac{V_w}{V_{void}}$$

Equation 3

where V_{void} is the volume of the void space (m^3). The degree of saturation ranges between 0 and 1, where 0 indicates that the pores contain no liquid and 1 indicates that the pores are fully saturated. Hence, full saturation is equal to the porosity of the medium. As the volume of water in the pores is most commonly less than the volume of pores in the unsaturated zone, the volumetric water content is usually less than the porosity ($0 < \theta < n$) and the water saturation is less than 1 ($0 < S < 1$) (Schwartz and Zhang 2003).

3.1.2 Flow in the unsaturated zone

The direction of flow in the unsaturated zone is determined by the gradient of the hydraulic head, h , which is defined as

$$h = z + \psi$$

Equation 4

where z is the elevation head (m) and ψ is the pressure head (m). Below the groundwater table, the pressure head is always positive and the flow is described by Darcy's law. Though the same concepts apply to flow in the unsaturated zone, some relevant differences need to be taken into consideration. The most important one is that the pressure heads are less than the atmospheric pressure, i.e. negative pressure. The pressure heads above the water table is also known as the suction head, acknowledging the matrix forces that bind water to solids in this zone (Domenico and Schwartz 1998). The flow proceeds vertically in the direction of decreasing hydraulic head; it moves upward due to evapotranspiration and matrix forces and downward in case of precipitation and water contents above the field capacity.

The suction and the volumetric water content of a pore strongly affect one another. This relationship can be expressed by a water retention curve (Figure 3-1), which is often described by the van Genuchten model

$$S_e = \frac{1}{\left[1 + (\alpha h)^n\right]^m}$$

Equation 5

where h is the matric potential (kPa) and α (kPa^{-1}), n and m ($m = 1 - 1/n$) are empirical parameters (Ghanbarian-Alavijeh et al. 2010). The parameter α is related to the grain size distribution of the soil and is a function of the matrix forces, while n and m describe the sorting grade of the sediments and the symmetry of the soil water retention curve, respectively. S_e is the effective saturation and is also expressed by

$$S_e = \frac{\theta - \theta_r}{\theta_s - \theta_r} \quad \text{Equation 6}$$

where θ_r is the *residual volumetric water content* (i.e. the lowest water content) and θ_s is the *saturated volumetric water content* (i.e. the water content when the pore is fully saturated)(Ghanbarian-Alavijeh et al. 2010). The van Genuchten model is often implemented to determine the pedotransfer functions for the volumetric water content and the hydraulic conductivities (Wösten et al. 1999). To determine the hydraulic conductivity, the van Genuchten model is coupled with the Mualem model in the van Genuchten-Mualem model and is given as

$$K(S_e) = K_s \left\{ S_e^l \left[1 - \left(1 - S_e^{n/(n-1)} \right)^{1-1/n} \right]^2 \right\} \quad \text{Equation 7}$$

The water retention curve portrays how the suction and the volumetric water content change as functions of one another. For instance, as the volumetric water content decreases, the suction increases simultaneously. When the water content increases however, that suction will decrease as a result. At both very high and very low volumetric water contents, small changes in water content leads to large changes in suction. At low water content, this is because soils never completely lose all of their water. The remaining water is the residual water content. The shape of the water retention curve depends on many factors, though the most important one is probably pore-size distribution (Domenico and Schwartz 1998). The shape of the curve also changes depending on whether the soil is wetting or drying, which is caused by *hysteresis*.

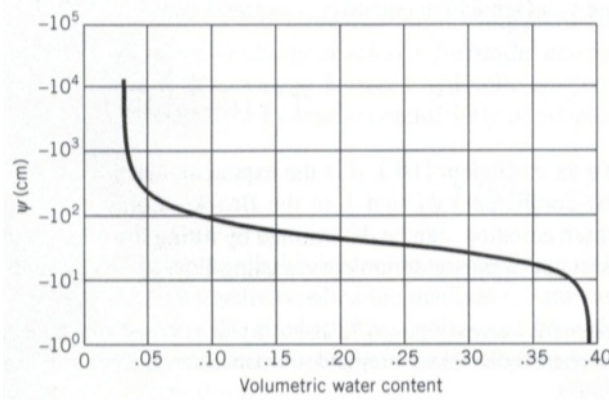


Figure 3-1: Suction plotted against the volumetric water content in a water retention curve (Schwartz and Zhang 2003).

Suction develops as pores start to desaturate. The first pores to empty are the largest, most conductive ones, leading flow only through the smaller pores that are still partially saturated. Hence, the preferred flow ways of the water changes as pores become available/unavailable due to changes in the state of the pore. If there is only residual water left in a pore, the pore is unavailable for water to flow through. This means that the medium's capacity to transmit water strongly depends on the degree of saturation (Schwartz and Zhang 2003). As the volumetric water content advances towards residual, it gets harder for water to move through the pores and the hydraulic conductivity decreases to a value close to zero. As the fraction of pores unavailable for flow increases, the water has to take a more difficult way to get through the soil than previously. The ratio of the average length of passages through water-filled pores is defined as *tortuosity* (Hillel 2004). As the number of pores unavailable for flow increases, the tortuosity increases simultaneously as the path through the interconnected pores is now longer than previously when the soil was more saturated (meaning that a higher number of pores was available for flow). If the medium contains an interconnected network of fractures, however, the fractures become the main pathway for fluid flow despite the unavailable pores (Schwartz and Zhang 2003).

The *Darcy equation* can be implemented to calculate flow in a saturated medium as

$$q = \frac{Q}{A} = -K \frac{h_1 - h_2}{\Delta l} \quad \text{Equation 8}$$

where q is the specific discharge (also termed the Darcy velocity)(m/s), Q is the volume of water (m^3/s) flowing through the cross sectional area A (m^2), K is the hydraulic conductivity (m/s), and $\frac{h_1 - h_2}{\Delta l}$ is the hydraulic gradient also known as i . The Darcy equation is a general equation that describes the flux of water in one dimension, x , through a homogeneous porous medium. However, it can also be used to describe flow in three dimensions as

$$q_{xyz} = \left(-K \frac{\partial h}{\partial x}\right) + \left(-K \frac{\partial h}{\partial y}\right) + \left(-K \frac{\partial h}{\partial z}\right) \quad \text{Equation 9}$$

where q_{xyz} is written as a partial differential equation for specific flow in the directions of the Cartesian coordinates x , y , and z (Appelo and Postma 2010). In the unsaturated zone, flow depends on the gradient of the suction head. Therefore, a modified version of the Darcy equation is valid for unsaturated flow – known as the *Darcy-Buckingham equation*. It is written as

$$q = -K(\psi)\nabla H \quad \text{Equation 10}$$

where ∇H is the hydraulic gradient that is influenced by both suction and gravitational components (Hillel 2004). $K(\psi)$ is the hydraulic conductivity as a function of the suction (m/s). It is a combination of the *relative hydraulic conductivity*, $K_r(\psi)$, and the *saturated hydraulic conductivity tensor*, K_s . This value for the hydraulic conductivity is a function of the degree of saturation, S , of the soil, which itself is a function of the suction, ψ , and can be written as

$$K(\psi) = K_r(\psi)K_s \quad \text{Equation 11}$$

The flow above the water table is in a transient state in a partially saturated body, and the laws of continuity and mass conservation are essential. In a relatively short time frame, the amount of water that enters the system is not necessarily equal to what exits it; the variance is expressed as the change of soil water storage. The principle of continuity

$$\frac{\partial \theta}{\partial t} = -\nabla q \quad \text{Equation 12}$$

can be combined with the Darcy-Buckingham equation in order to describe transient flow in the unsaturated zone and how the volumetric water content changes over time, t . This equation, the *Richard's equation*, can be written as

$$\frac{\partial \theta}{\partial t} = \nabla(K(\psi)\nabla H) \quad \text{Equation 13}$$

where ∇ is the *vector differential operator*. It represents the three-dimensional gradient of the flux q (Hillel 2004).

3.1.3 Infiltration in the unsaturated zone

Water may enter into the soil under a variety of conditions, and this process of water entry into the soil is termed *infiltration*. It generally occurs by downward flow through all or part of the soil surface (Hillel 2004). The fraction of the water that enters the root zone compared to what runs off is determined by the rate of infiltration, i.e. the volume flux of water flowing into the profile per unit of soil surface area. Infiltration can be limited by soil conditions such as initial wetness and suction, as well as texture, structure, and uniformity of the profile, which may lead to plants being denied sufficient moisture as well as increased surface erosion (Hillel 2004).

3.2 Soil compaction

3.2.1 Compaction in theory

Hillel (2004) refers to *compaction* as the densification of an unsaturated soil as a result of the reduction of the fractional air volume. In dry conditions, the soil particles are typically strongly bound together and, as a result, are able to resist compaction. As the soil wetness increases, however, the bonds between the soil particles are weakened, and the soil is more likely to experience compaction. The bulk density after compaction is a function of soil wetness. Starting from a dry condition, the bulk density increases as the soil is wetted and the moisture content increases. It reaches a maximum density at a wetness termed *optimal moisture* (Hillel 2004). The fractional air volume of the soil is simultaneously reduced as the

soil wetness approaches saturation. This results in the soil being unable to be compacted to the same degree compared to at lower moisture contents. Therefore, an increase in moisture content beyond the optimal moisture reduces, rather than increases, soil compactibility. For continued compaction, pore water has to be removed. At high moisture content, the water prevents a closer packing of the soil particles as it pushes the grains apart and causes swelling (Hillel 2004).

3.2.2 Compaction in agriculture

In agricultural soils, the soil is considered compacted when the total porosity is so low that it restricts aeration or when the pores are so small that it restricts root penetration, infiltration, and drainage (Hillel 2004). Such compaction might take place as a result of the influence of man-induced mechanical forces, especially vehicular activity, that are applied at or near the soil surface. For clayey soils, it is especially damaging when the soil has a high moisture content and a resulting low strength. Deep rutting, smearing, and compaction can arise when harvesting in wet conditions, which might inhibit infiltration, drainage, and aeration of the soil (Hillel 2004). In modern agriculture, it is common that the use of heavy machinery increases the bulk density in the deeper soil layers, usually below 25 cm depth, while decreasing the bulk density in the upper soil layers (Bouwman and Arts 2000).

3.3 *Electrical resistivity*

Electrical resistivity is defined as the soil matrix' ability to resist conducting an electrical current (Schwartz and Zhang 2003). As pointed out by Samouëlian et al. (2005), the resistivity of the soil is a function of a number of soil physical properties, including soil structure (i.e. particle size distribution and mineralogy), arrangement of voids (i.e. porosity, pore-size distribution, and connectivity), the degree of water saturation (i.e. water content), electrical resistivity of the fluid (i.e. solute concentration), and temperature. It can be considered as a proxy of many physical properties, including soil structure, water content, and fluid composition. When measuring the resistivity across a field area, it can determine how such physical properties vary spatially and temporally across the area (Samouëlian et al. 2005).

3.3.1 Basic principles

Rocks and sediments conduct electrical currents in three different ways: (1) Electrolytic conduction, which occurs as a consequence of the ions in the pore water solution; (2)

dielectric conduction, which occurs due to the charged layer present on so-called insulators (e.g. clay minerals); and (3) electronic conduction, which occurs when electrons move rapidly through metallic substances and, that way, carry the charge (Reynolds 2011). Electrical resistivity, a fundamental and diagnostic physical property, indicates the resistance of a material to conduct electrical currents. The basic definition of resistivity is illustrated in Figure 3-2.

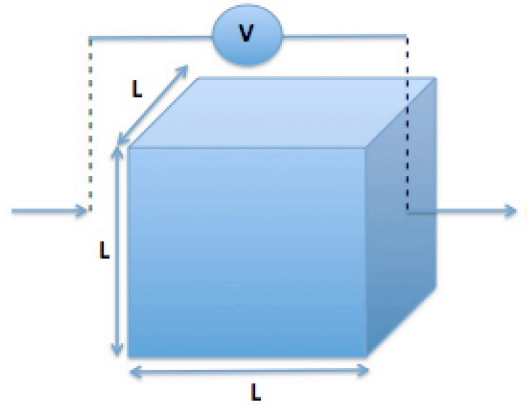


Figure 3-2: A sketch of the simple definition of resistivity across a cube with side length L with an applied current I and the potential drop between opposite sides V (adapted from Reynolds (2011)).

When a current, I , is passing through a cube with side length L , the material within the cube resists the current, which leads to a drop in potential, V , between the opposing sides. Resistance, R (Ω), of the cube is proportional to the length, L (m), while it is inversely proportional to the cross-sectional area, A (m^2), of it. The constant of proportionality is termed the “true” resistivity (Reynolds 2011), and can be written as:

$$R = \rho \frac{L}{A} \quad \text{Equation 14}$$

Ohm’s Law states that the resistance, R , of the cube is also defined by the ratio of the electric potential, V (V), to the applied current, I (A), as:

$$R = \frac{V}{I} \quad \text{Equation 15}$$

Resistivity is a product of the combination of the two previous equations, as

$$\rho = \frac{VA}{IL} \quad \text{Equation 16}$$

measured in ohm-meters (Ωm).

Of all the physical properties of geological materials, resistivity exhibits one of the largest ranges. What resistivity the material has depends on, among other factors, the type, age, and porosity of the rock. Of the main types of rocks, the sedimentary rocks tend to have the highest resistivities (Reynolds 2011). Compaction of the rocks causes a decreased porosity and permeability. As conduction occurs through pore fluid acting as electrolytes in most rocks, this leads to a lower conduction and increased resistivity (Reynolds 2011).

3.3.2 In the field

Electrical resistivity tomography (ERT) is a non-intrusive, active geophysical method that is implemented to measure the Earth's resistivity. As water is mostly electrically conductive, the resistivities provided through ERT are primarily controlled by the amount of water content and the concentration of dissolved solids within the soil matrix (Afshar et al. 2015). Hence, it is possible to gain information about the subsurface and the different types of soils and layers it consists of, as well as to explore the groundwater.

When applying ERT to determine the resistivity of the subsurface, it is not the true resistivity that is obtained, but the *apparent resistivity*, ρ_a (Ωm), as the subsurface is not a homogeneous medium like in Figure 3-2. Apparent resistivity is the product of a measured resistance, R (Ω), and a geometric factor, K (m), for a specified line of electrodes. The apparent resistivity changes according to the relative position of these electrodes (Samouëlian et al. 2005). The resistance can be measured if a known electrical current, I , is inserted through a pair of current electrodes and the electrical potential, δV , is measured between a pair of potential electrodes, as

$$R = \frac{\delta V}{I} \quad \text{Equation 17}$$

The geometric factor is defined by

$$K = 2\pi \left[\frac{1}{AM} - \frac{1}{MB} - \frac{1}{AN} + \frac{1}{NB} \right]^{-1} \quad \text{Equation 18}$$

where A and B represent two current electrodes, while M and N represent two potential electrodes. The resistivity that is calculated, the apparent resistivity, is defined as a combination of the two previous equations, as

$$\rho_a = RK \quad \text{Equation 19}$$

It is the geometric factor that takes into account the spreading of the electrodes (i.e. the distance between them), which varies with different configurations of electrodes. The main electrode configurations used in electrical surveys are Wenner, Schlumberger, Dipole-Dipole, and Square (Reynolds 2011). What configuration is the most suitable depends on different criteria that are set for the investigation.

3.4 Computer modelling and analysis

3.4.1 Geostatistical analysis with SGeMS

SGeMS is a geostatistical modelling software developed at Stanford University, USA. By implementing geostatistical algorithms, it allows the user to model earth systems and space-time distributed phenomena (Remy et al. 2009). It was developed with the goal of offering a large range of geostatistical tools that are easy to use.

For this thesis, SGeMS was used to quantify the spatial variance through the creation of variograms, which is a graphical visualization of the correlation between data points. A variogram is a coordinate system consisting of semivariances, i.e. measures of the degree of spatial dependence (Davis 1983), between data points. The semivariances is defined as

$$\gamma_h = \frac{1}{2n(h)} \sum_i^{n(h)} (X_i - X_{i+h})^2 \quad \text{Equation 20}$$

where γ_h is the semivariance at distance h between points. X_i and X_{i+h} are the regionalized variables taken at location i and at h distance from i , respectively; and $n(h)$ is the number of comparisons between pairs of points (Oliver and Webster 2014). When calculating the semivariance between points at different distance intervals (e.g. 1-2 meters and 2-3 meters), the resulting values can be plotted into a variogram to see how the data is correlated and at what distance the data points are no longer correlated. By implementing the variogram to find an optimal set of weights to estimate unsampled points, Kriging can be used towards creating contour maps with a measure of the error or uncertainty of the surface (Davis 1983).

3.4.2 Simulation of water flow with HYDRUS

HYDRUS is a graphical computer platform for simulating water, heat, and solute movement in one, two, and three dimensions. (Šejna et al. 2014). By numerically solving the Richard's equation for water flow and convection-dispersion type equations for heat and solute transport, HYDRUS is able to analyse water and solute movement in variably saturated porous media (Šimůnek et al. 2012). It was developed to simplify the process of transforming complex data sets into graphical representations, and the computational codes are hence directly connected to the interface.

As stated by Šimůnek et al. (2012), HYDRUS calculates the hydraulic properties water retention, $\theta(h)$, and hydraulic conductivity, $K(h)$, by the use of either of the analytical models created by Brooks and Corey (1964), Mualem-van Genuchten (1976/1980), Vogel and Císlerová (1988), Durner (1994), and Kosugi (1995). By implementing a scaling procedure, HYDRUS can include spatial variability of these properties in the flow domain (Šimůnek et al. 2012).

In this thesis, HYDRUS Version 2.04 has been employed to simulate flow in the unsaturated zone. The flow has been parameterized with the van Genuchten model, though scaling of variable hydraulic conductivity has been neglected.

4 Methods

4.1 *Electrical resistivity tomography*

In SOILSPACE, electrical resistivity tomography (ERT) was chosen to explore how the resistivity varies spatially and to determine what part of the plot is most interesting for further investigations.

To characterize the spatial heterogeneity of the field area, 24 ERT lines were laid out 0.5 meters apart. 48 electrodes were connected to each of the lines, also with the spacing of 0.5 meters. This grid size was chosen to cover the area while still gaining detailed information close to the surface. The ERT cable was connected to the measuring device Syscal Pro, produced by Iris Instruments. Figure 4-1 shows the ERT lines in the field area, while Figure 4-2 shows close ups of an ERT cable with its electrodes.

The Wenner and Dipole-Dipole configurations were chosen to achieve good horizontal and vertical resolution, respectively. A combination of the two leads to better interpretation as it enhances the chance of reading different features of the subsoil (Samouëlian et al. 2005). They were used in both the normal and the reciprocal configurations, the latter meaning that the current and potential electrodes are swapped.

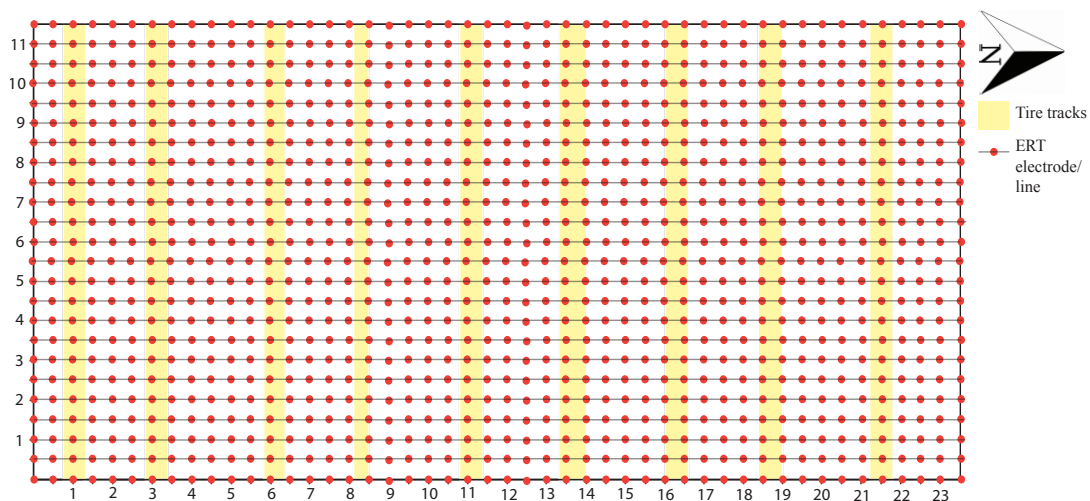


Figure 4-1: The layout of the ERT lines, in meters. Each red dot represents an electrode. Created with Adobe Illustrator.



Figure 4-2: Image (A) shows how the ERT cable had to be laid out for the electrodes to have a spacing of 0.5 meters and (B) shows an electrode and how it is connected to the cable. Photo: Andrea Nymo Fikse.

A time-lapse ERT measurement was also implemented throughout the winter season of 2015/2016, with the Wenner configuration, to explore how the resistivity varies temporally and with change in climatic conditions. If assuming the ionic concentration in the water is constant, the electrical resistivity of the soil will change over time as a result of fluctuating soil moisture content and soil water conductivity (French and Binley 2004). The time-lapse ERT will indicate how the increased infiltration changes the flow paths in the unsaturated zone, especially as the infiltration rate varies spatially. This has previously been done by French and Binley (2004) to describe the variability of infiltration during snowmelt. The sequence was implemented at $X = 0-23.5$ and $Y = 2$. The resistivity was measured a number of times from December 3, 2015, to April 1, 2016.

As a result of the ERT measurements, fellow researchers on the SOILSPACE project set aside an 8m x 7m square in the Southwest corner for other purposes. The following methods were performed on the remaining plot area.

4.2 Dielectric water potential sensor and TDR sensor

The purpose of a dielectric water potential sensor is to log the suction in the unsaturated zone. The sensor used here, produced by Decagon Devices, was the maintenance-free MPS-2 Dielectric Water Potential. It also measures the temperature in the ground, making it suitable to determine suction in partially frozen soils (DecagonDevices(1) 2015). Before going out

into the field with this sensor, it was subjected to water the night before to make sure it was fully saturated.

The purpose of a TDR sensor is to measure the soil’s moisture content. The sensor used, also produced by Decagon Devices, was the 5TM Moisture and Temperature Sensor. By measuring the dielectric constant, it determines the volumetric water content of the soil (DecagonDevices(2) 2015). No preparations had to be done with this sensor.

The purpose of measuring the suction and the moisture content is to contribute to the understanding of how they are connected and affect one another. Measurements were taken every two meters in each direction, as shown in Figure 4-3. Both of the sensors were plugged into Em50-series data loggers (Figure 4-4).

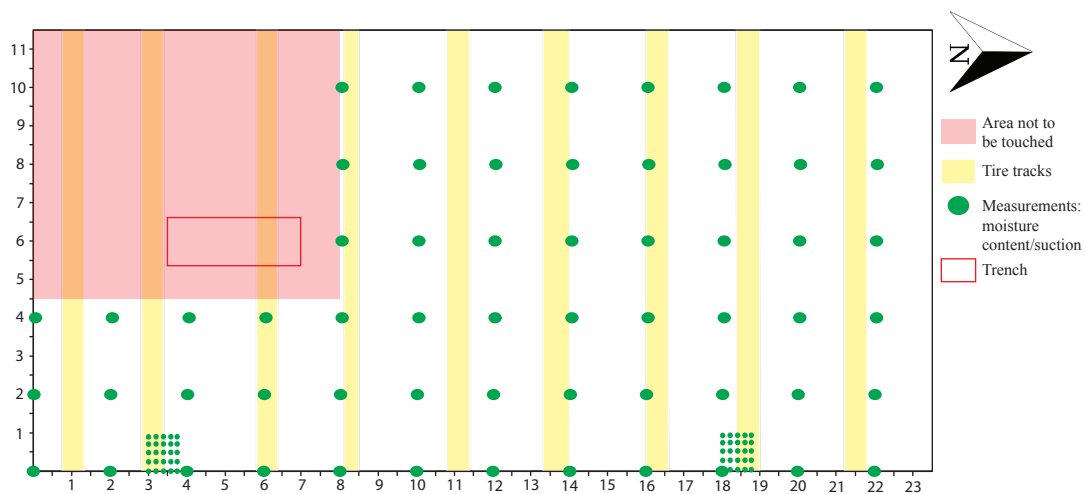


Figure 4-3: Moisture content and suction was measured every two meters in each direction, as well as every 20 centimetres in two squares as portrayed in the image. The data from the two smaller squares was to be used in calculating spatial variability. Created with Adobe Illustrator.

The dielectric water potential sensor and the TDR sensor were placed approximately five centimetres apart to avoid them affecting one another. Each of the data loggers was connected to a computer to start the measurements. An interval of 1 minute was set for both loggers. The loggers measured on each location for 20 minutes, giving the sensors enough time to stabilize.

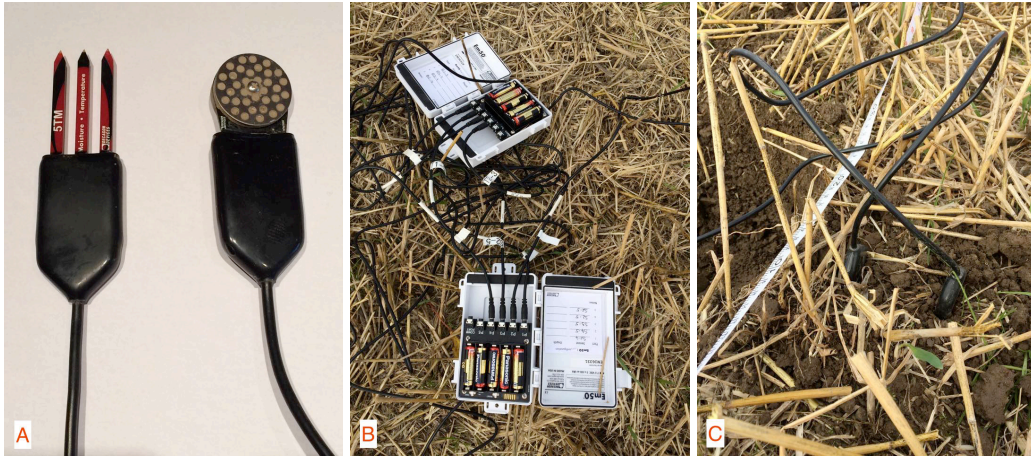


Figure 4-4: The TDR sensor and the dielectric water potential sensor (A) connect to data loggers (B). They were pushed into the ground approximately five centimetres apart (C). Photo: Andrea Nymo Fikse.

4.3 Double-ring infiltration test

Infiltration tests were performed both on and between tire tracks from the agricultural vehicles, based on the method described by Børresen and Haugen (2003), to contribute to the understanding of how the vehicles affect the soil and its infiltration rate. Double ring infiltration tests were carried out on three different locations within the field area. In each location, one infiltration test was performed on a tire track, while the other infiltration test was performed between the tracks, as seen in Figure 4-5.

Two sets of rings were implemented simultaneously, where one set had rings with diameters of 0.325 and 0.540 m, while the other set had rings with diameters of 0.285 and 0.540 m. For each test, two metal cylinders of different sizes were subjected into the ground – the larger surrounding the smaller. Water was added to both rings; first to saturate the ground, and then to conduct the measurement of the infiltration rate. The height of the water in the smaller ring was measured until all the water in the larger ring had infiltrated.

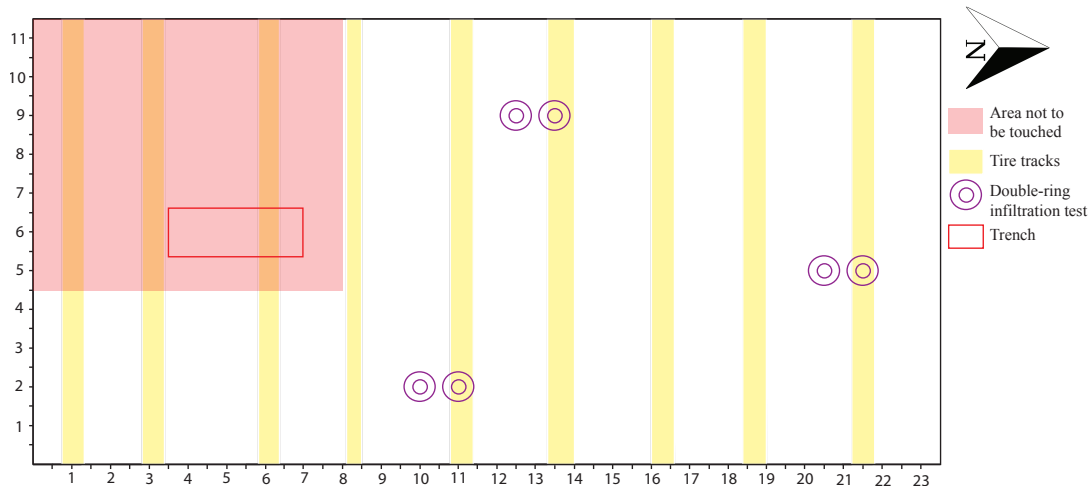


Figure 4-5: Six double-ring infiltration tests were performed, where three of them were on tire tracks, while the remaining three were between tire tracks. Created with Adobe Illustrator.

Calculations

The rate of infiltration was determined with the help of Darcy’s equation. The infiltration rate, which in this case is the same as the Darcy velocity, was calculated by dividing the height of the water at the initial time step with the total time it took for the water to infiltrate. As the infiltration is assumed to be vertical, the hydraulic gradient, i , is equal to 1. Hence, the infiltration rate is equal to the saturated hydraulic conductivity, K_s .

4.4 Sounding

A sounding test was performed at the location (4,2) in the field plot with the use of a jackhammer and filled iron pipes. The aim was to estimate the depth to the bedrock as well as to gain information about different types of materials that might exist beneath the surface. A total of eleven pipes were implemented during the test. The jackhammer subjected the pipes into the ground; every 0.5 meters, a sounding test was conducted by rotating the pipes with the use of two adjustable wrenches. The rotation ought to provide clues as to what the material surrounding the end-piece might exist of. Fine materials such as clay and silt might not cause any sounds, while larger grains such as sand and gravel might cause a louder scraping noise. Hence, it is possible to interpret the soil type based on the scraping noise. The sound was noted and the type of soil was interpreted, before the pipes were subjected another 0.5 meters into the ground and the pipes were rotated again. This procedure was repeated until bedrock was reached.

4.5 Sediment sampling

Sediment samples are valuable for determining soil physical parameters used in model simulation of water flow. Hence, sediment samples were collected from a total of 55 locations in the field plot (Figure 4-6). Approximately every three meters, two soil samples were collected with the traditional steel cylinders (100 cm^3): one to go through a pF-analysis, while the other to determine the volumetric water content at the time it was collected and the grain size distribution. Figure 4-7 illustrates how these samples were collected from the field using a hammering head and a hammer. The steel cylinders were capped with red lids to avoid evaporation before being analysed for pore volume, bulk density, and water retention characteristics. Sediment samples were also collected with a shorter distance interval, i.e. every 1 m within two squares, and from different depths within the trench, i.e. at 0.17, 0.34, and 0.52 m below the surface, to investigate the spatial variance of the grain size distribution.

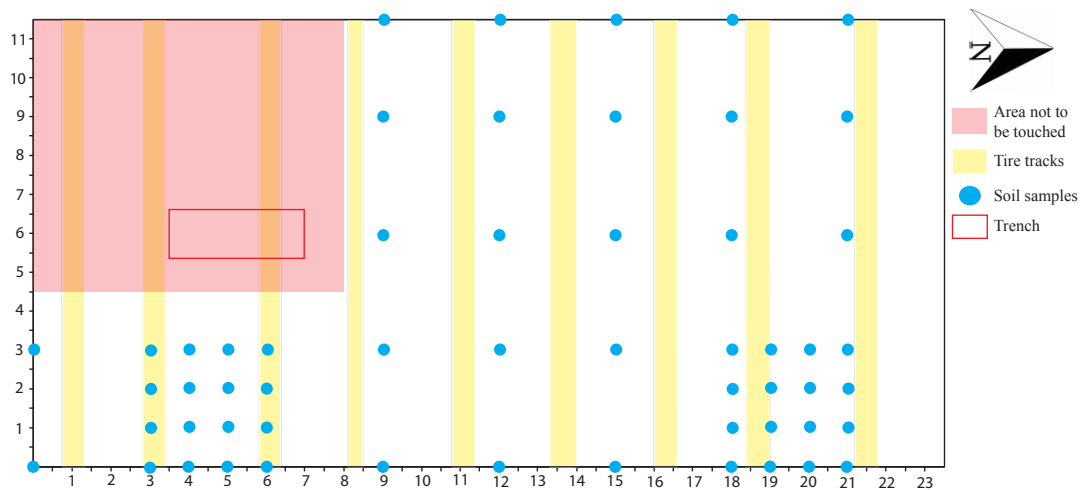


Figure 4-6: The researched field plot in meters, including the locations for the soil samples. Two sediment samples were collected every three meters in each direction. In the two smaller plots, only one sample was collected from each location to be used towards spatial variability. Created with Adobe Illustrator.



Figure 4-7: The steel cylinder had to be completely filled with soil, as shown in (A). To achieve this, a hammering head, as is shown in (B), was put on top of the ring before applying a hammer to beat the ring into the ground. Photo: Andrea Nymo Fikse

4.6 Sediment sample analysis

4.6.1 Grain size distribution

Grain size distribution of a few dry samples with the use of sieves with sizes 0.0063, 0.125, 0.25, 0.6, 1, and 2 mm determined that more than 70% of the grains are smaller than 0.0063 mm. Hence, the grain size distribution analyses were performed according to the procedure described by Krogstad et al. (1991) and Rygalska (2015). Through this procedure, the soil samples were separated into fractions ranging from clay to coarse silt with the pipette method, and into fractions ranging from fine to coarse sand by subjecting the remaining sample through different sized sieves.

The pipette method determines the grain size distribution of the sample as a result of different sedimentation rates for different sized particles, as describes by Stokes law:

$$v = \frac{\mu_s - \mu_w}{18\eta} g d_e^2$$

Equation 21

where v is the sedimentation velocity of a spherical object, μ_s and μ_w are the density of the soil particles and of water, respectively, d_e is the effective particle diameter, g is the gravitational force, and η is the water viscosity.

Prior to the analysis, the samples were pre-treated to remove organic material and separate grains. 10 g of each sample were brought into suspension. 35% H_2O_2 was added to cause oxidation of organic matter, both with and without the influence of heating. The amount of H_2O_2 necessary depends on the amount of organic matter in the sample. Due to the high amount in these samples, it was added thrice.

When the organic matter was oxidized, the samples were washed with distilled water and dispersed by addition of the chemicals 2 M HCl and 0.05 M $\text{Na}_4\text{P}_2\text{O}_7$. The suspensions, dispersed and oxidized, were then transferred to 400 ml cylinders and ready for the pipette method, performed by the NMBU-IMV department engineer Magdalena Rygalska. The temperature of the solution in the cylinders was measured with an accuracy of 1 °C to calculate the sedimentation time of the different soil particle fractions. The sample solutions were mixed thoroughly to secure suspension of all of the soil particles. With the pipette, 20 ml of suspension was extracted at different time intervals, as previously determined by the temperature of the suspension. Grain sizes from clay to coarse silt were removed this way. The remaining of the suspensions was subjected through sieves of sizes 600 μm , 212 μm , and 63 μm to determine the sand fractions. The samples were dried at 105 °C and the weight of each fraction was noted.

The pre-treatment and the pipette method were performed on a total of 55 sediment samples from the field area. 10 samples were treated simultaneously.

Calculations

The weight of the salts from the dispersion liquid was subtracted from the sample weight. As the volume of the pipette is 20 ml, the weight of each pipetted sample was multiplied by 20 to estimate the total weight of that fraction in the 400 ml suspension. As the sand fractions were separated through sieving, the resulting weights represent the total weight of the respective fraction. The total weight of the sample was calculated by summarizing the individual weight fractions, W_i . This value is always less than 10 g as organic matter has

been oxidized in the pre-treatment of the analysis. The weight % of each fraction was determined with

$$\frac{W_i}{\sum W_i} \cdot 100\% \quad \text{Equation 22}$$

The soil samples were classified according to the USDA (1993) soil texture triangle from the relative composition of sand, silt, and clay.

4.6.2 Water retention characteristics

Water retention characteristic (pF), air capacity, porosity, bulk density, air permeability, and hydraulic conductivity can all be determined with the so-called pF-analysis. The 31 sediment samples in the steel cylinders were covered with nylon cloths at the bottom to avoid loss of sample. The samples were fully saturated at the beginning of the analysis. Throughout the analysis, the samples were subjected to 5 kPa (ψ) in the sandbox and 10, 100, and 1500 kPa ($-\psi$) at ceramic plates in a pressure chamber. When reaching equilibrium at each suction/pressure level, the weight of the samples was noted before being subjected to the next suction. The samples were then dried at 105 °C and weighed. After being subjected to a pressure of 10 kPa, the samples were analysed for air capacity and air permeability with an air pycnometer and an air permeameter, respectively. For the last pressure, i.e. 1500 kPa, the sediment samples were ground and grains larger than 2 mm were removed. Part of the dried samples were transferred to smaller cylinders, saturated, and placed in a pressure chamber to determine the wilting point, which is defined as the volumetric water content at this specific suction. The samples were in the chamber until they reached equilibrium. The samples were weighed both wet and dried.

Sandbox

At the first stage of the analysis, the samples were placed in a sandbox; a box filled with sand and covered with a nylon cloth. The nylon cloth was there to avoid the sand in the box and the sediment in the samples to mix. Connected to the box was a tube in which the water extracted from the samples was led through. Each cylinder was pressed slightly into the sand to improve soil-sand contact (Børresen 2011). The pressure regulator was put at 50 cm head and the lid was placed on top of the box to eliminate evaporation. The water extracted from

the box was measured in a measuring cylinder. That the system had reached equilibrium was evident from the stabilizing of water in this cylinder.

Pressure chamber

During the remaining levels of suction, the cylinders were placed on saturated ceramic plates and put in a pressure chamber. Tubes were connecting these plates to the pressure chamber. When subjected to suction, water in the sediment samples was extracted and led through the ceramic plates through this tube and out of the pressure chamber. A measuring cylinder was attached to the outside of the chamber to measure the amount of water extracted. When the water in the cylinder had stabilized, the system had reached equilibrium.

Air pycnometer

The air pycnometer measured the air capacity of each sample, i.e. the volume of air in the sample. When measuring, a cylinder was placed in the measuring chamber and the cock was opened for pressure. When the pressure gauge showed 1000, the cock was turned so that the measuring chamber was connected to the pressure gauge. The pressure was noted when stabilized (Børresen 2011). The apparatus was calibrated by the use of steel disks with known volumes. By removing one disk at a time from the cylinder, values were gained for specific volumes, which were later used to calibrate the values gained when measuring the air capacity of the sediment samples.

Air permeameter

The air permeameter was implemented to measure the air permeability of each sample, i.e. the flow of air (Børresen and Haugen 2003). The permeameter was connected to a compressor and two vents controlled the amount of air released through the apparatus. When opened, the air was led to a framework with three Platon airflow gauges with different areas of measurements. One of these gauges was to be open at all times. The apparatus was further connected to a water column, with the air pressure being at 15 cm. Each of the samples were placed in the air permeameter and subjected to air released from the compressor. The amount of air released was adjusted in order to stabilize the water in the water column at 15 cm. The airflow was noted from the active gauge.

Calculations

A weight loss of 1 g equals 1 cm³ as the cylinders each have a volume of 100 cm³ and the density of water is 1. The weight of the sample at a certain suction subtracted by the dry weight of the sample determined the water content in the sample at that suction level. The bulk density was found by subtracting the weight of the empty cylinder (i.e. the weight of the cylinder and two lids) from the gross weight of the sample, and then dividing it with the volume of the cylinder. The pore volume was determined by adding the water and the air volume (from the air capacity test) at suction 10 kPa. The particle density was found by dividing the net dry weight of the sample on the material volume (i.e. 100 – pore volume). When determining the water content at the wilting point, it was first calculated as weight % loss of water. This value was then converted to volume % water content by multiplying it with the dry bulk density of the soil sample.

The resulting volumetric water content for each suction level were plotted as water retention curves, where the suction was plotted as pF values ($-\log_{10}(\psi)$). The van Genuchten parameters θ_s , θ_r , α , and n were found for each pF curve with use of the volume % water content at each suction level and at saturated condition. The SWRC Fit web interface produced by Seki (2007) calculated these parameters.

The air permeability was used to estimate the hydraulic conductivities of the plot. First, air permeability was converted to water permeability with the equation

$$k_w = 0.106 \cdot k_a^{1.31} \quad \text{Equation 23}$$

where k_w is the permeability of water and k_a is the permeability of air, both in μm^2 (Riley 1996). The water permeability was further converted to the hydraulic conductivity through

$$K = \frac{k \rho_w g}{\mu} \quad \text{Equation 24}$$

where the density, ρ_w , and dynamic viscosity, μ , of water are 998.2 kg/m³ and 1.002E-3 kg/(m sec), respectively (Schwartz and Zhang 2003).

4.7 *Computer modelling*

4.7.1 **SGeMS**

Histograms, variograms, and Kriged maps were created for 15 of the resulting parameters from the pF analysis, the measuring of water characteristics in the field, and the grain size distribution analysis.

Variogram

The variograms were created with the purpose of determining the spatial correlation in different directions and to function as weights when creating the Kriged maps of the parameters. The variograms of the total field plot consist of ten lags with a separation of two or three meters (depending on the separation between the sampling) and a tolerance of one meter. Five variograms were constructed for each parameter. One of the variograms was omnidirectional (with an angular tolerance of 90° and a very large bandwidth), while the remaining four were directional (at 0, 45, 90, and 135°, each with an angular tolerance of 22.5° and a bandwidth of 100 m). For each variogram, the sill was set at the variance value determined when producing the histogram for that specific parameter.

Kriging

Kriged maps were created for all of the parameters with the use of the variograms described above. The kriging type *Simple Kriging* was chosen to produce the maps as recommended by Remy et al. (2009) due to the Gaussian simulation theory. The mean value given in the histogram of each parameter was added. For the larger maps, it was required to use between 2 and 12 of the nearest neighbouring points found in a radius of 30 meters to estimate each grid point. For the smaller maps, the radius of the search ellipsoid was reduced to ten meters.

4.7.2 **HYDRUS**

Two 2D models have been created of the field plot in Skuterud. They are both vertical cross-sections with the intention of inspecting how skewing of the model, the occurrence of both topsoil and subsoil compaction, and drainage tiles affect the vertical movement of water. Both models were created with HYDRUS 2.04. The single porosity hydraulic model van Genuchten-Mualem describes the soil water characteristics with the assumption that there is no hysteresis occurring, and the van Genuchten parameter n was defined based on the values given by SWRC Fit. The solute flow parameters are assumed to be depending on water

content, as well as affected by a tortuosity factor according to the formulation by Millington and Quirk (1961). The Millington and Quirk model is frequently used to estimate the *effective diffusion coefficient*, D_i , for solute transport, and is given by

$$D_i = \frac{D_f \theta^{10/3}}{n_e^2} \quad \text{Equation 25}$$

where D_f is the free-water diffusion coefficient (Saripalli et al. 2002).

The material is defined as silt loam based on the results from the grain size distribution analysis, while the bulk density is defined as the average value of the resulting values from the water retention characteristics analysis.

The parameters not mentioned in this chapter have the defaulted values provided by HYDRUS.

Conceptualization

The 2D models are vertical cross sections of the field plot in the north-south direction. They are defined in a 2D general domain and stretch two meters in the horizontal direction and one meter in the vertical direction. A tile drain is included approximately in the middle of each model at 0.8 meters depth with a radius of 0.05 meters. The models are divided into two layers where the top layer, with thickness of 0.3 meters, represents the plough layer. The models' designs are symmetrical with tire tracks on both ends of the top layer. The deeper layer has a thickness of 0.7 meters and is assumed to be homogenous. Both models have hydraulic gradients of 0.022 as given by GNSS measurements. The models are further divided into meshes consisting of elements sized 0.2 m by default. Each model has 1367 nodes, 156 1D-elements, and 2614 2D-elements.

In one of the models, there is only topsoil compaction, while in the other there is both topsoil and subsoil compaction. The value for hydraulic conductivity is less in the compacted parts of the models. This conductivity is a calculated value derived based on information from the double-ring infiltration tests and the water retention characteristics analysis. The hydraulic conductivity determined through the water retention characteristics analysis was divided by the difference between the hydraulic conductivities on and off tire tracks determined with the

infiltration tests to find the assumed value of the compacted areas implemented in this model. In the remainder of this thesis, the 2D vertical cross-sections with and without subsoil compaction are referred to as *Cross-Section 1* and *Cross-Section 2*, respectively.

The ground surface of the models have the boundary condition atmospheric boundary, the drainage tiles have the boundary condition free drainage, and the base and sides of the models have the defaulted boundary condition no flux.

Simulations

The two models each simulate flow of water and spreading of a tracer. Precipitation data, provided by eKlima (2016), from the measuring station at Rustadskogen in Ås from January, July, and November of 2014 (Appendix B) was used as boundary conditions when running the simulations. These months have been chosen due to the variation in precipitation patterns. In January, for instance, there was a dry period lasting 17 days, while the month of November can be characterised as rather wet with only six days without any precipitation and its longest precipitation period lasted for 14 consecutive days. In July, however, the precipitation periods were small and rather evenly spread out with increased precipitation at the beginning and the end of the month. In the remainder of this thesis, January, July, and November are referred to as M1, M2, and M3, respectively. For all the three months, other climatic conditions, including temperature, are assumed to be constant. Examining the flow of water through these three months will then reveal how different amounts of infiltrating water might affect the flow during otherwise equal conditions. A tracer with concentration 1 mmol/m³ was added with the incoming flux a day prior to the start of each month with a total precipitation of 0.01 m during this day to be able to trace the flow ways. This was to make sure that equal amounts of tracer were added in each scenario. Hence, each simulation lasted for a total of 32 days.

To be able to create breakthrough curves of the tracer, a tracer plume was added close to the surface in the middle of both of the models with an initial concentration of 0.5 mmol. The tracer that was coming in with the precipitated water was then removed. The three scenarios were adjusted to last 60 days with 0.01 m incoming precipitation each day after day 32 with the intention of removing the tracer from the system.

Additionally, M3 was modelled to investigate the rate of water movement from different parts of the cross-section. Tracer plumes were added to three locations close to the surface in Cross-Section 2 and the movement of each tracer was examined.

The aim of the 2D simulations was to answer the following questions:

- How does different saturated hydraulic conductivities affect the infiltration during the three months?
- Do the simulations show any effect of the tire tracks?
- To what degree is the flow of water affected by the tilting of the models?
- How long does it take for the infiltrating water to reach the tile drains?
- In what way do the tile drains affect the flow of water?

5 Results

5.1 *Electrical resistivity tomography*

The objective of the electrical resistivity tomography that was performed to cover the field plot was to aid in selecting a smaller area for further analysis in the SOILSPACE project. The resulting images are given in Appendix C.

For this thesis, the ERT time-lapse measurements are more interesting as they portray changes in resistivities with temporally varying water contents. The first measurement was on 03/12/2015, and the last on 01/04/2016. In Figure 5-1, the temperature and incoming precipitation is shown for the period of measurements. Measurements were taken a number of times during this period, though not all resulted in useful data. The best data sets are from the measurements taken on 03/12/2015, 14/01/2016, 26/01/2016, 29/01/2016, 12/02/2016, and 01/04/2016, and the label ERT in the graph point out these measurements relative to the climate.

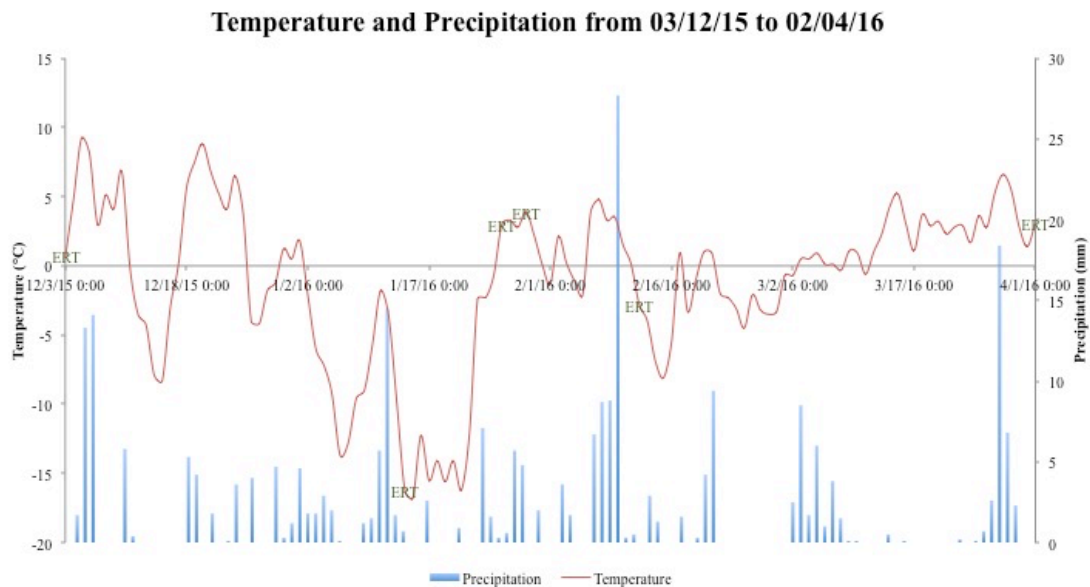


Figure 5-1: The changes in temperature in °C and the incoming precipitation in millimetres from 03/12/2015 to 01/04/2016. Included on the temperature graph are labels named “ERT” to point out when the measurements were taken relative to the climatic situation.

Between 03/12/2015 and 01/04/2016, the temperature fluctuated greatly with the minimum and maximum temperature being -16.8 and 9.2 °C, respectively. The minimum temperature coincides with the measurement on 14/01/2016. Figure 5-1 illustrates the occurrence of peaks in both temperature and precipitation prior to the ERT measurements on 14/01/2016, 12/02/2016, and 01/04/2016, though the temperature remained below zero before the measurement on 14/01/2016 despite the great increase. Especially before the measurement on 12/02/2016, Figure 5-1 portray how there had been a large period of precipitation prior to the measurement that theoretically ought to affect the resistivity negatively. There was a great increase in temperature between 14/01/2016 and 26/01/2016, but, according to senorge.no (2016), no melting of the snowpack had occurred between the two measurements. Between the measurements on 26/01/2016 and 29/01/2016, melting of the snowpack caused 17 mm of water to infiltrate (senorge.no 2016), which would theoretically reach 17 cm into the ground if moving at a steady pace. In Table 5-1, the temperature on the days of measurement and the precipitation of the previous seven days are given, which will be helpful in the interpretation of the ERT images. Based on this data, great variations between the measurements might not be expected.

Table 5-1: The dates of measurement with the temperature of that specific day and the incoming precipitation of the previous seven days.

Date of measurement	Temperature °C	Precipitation during the previous seven days mm
03/12/15	0.7	24.3
14/01/16	-16.2	25.3
26/01/16	3	9.9
29/01/16	3.9	20.1
12/02/16	-2.8	52.7
01/04/16	3.1	30.9

5.1.1 Absolute resistivity images

The resulting images from the time-lapse measurements are given in Figure 5-2. The images portray absolute resistivities given on a linear scale. As the focus in this thesis has been on the topmost part of the soil profile, each of the images has been cut to display the top meter of the ground. Tire tracks are marked with stapled lines to be able to evaluate whether there are any connections between the areas compacted by vehicular activity and the resistivity

Results

values. The images show a range of resistivities from less than 43 to more than 222 Ωm , which suggests rather homogeneous conditions.

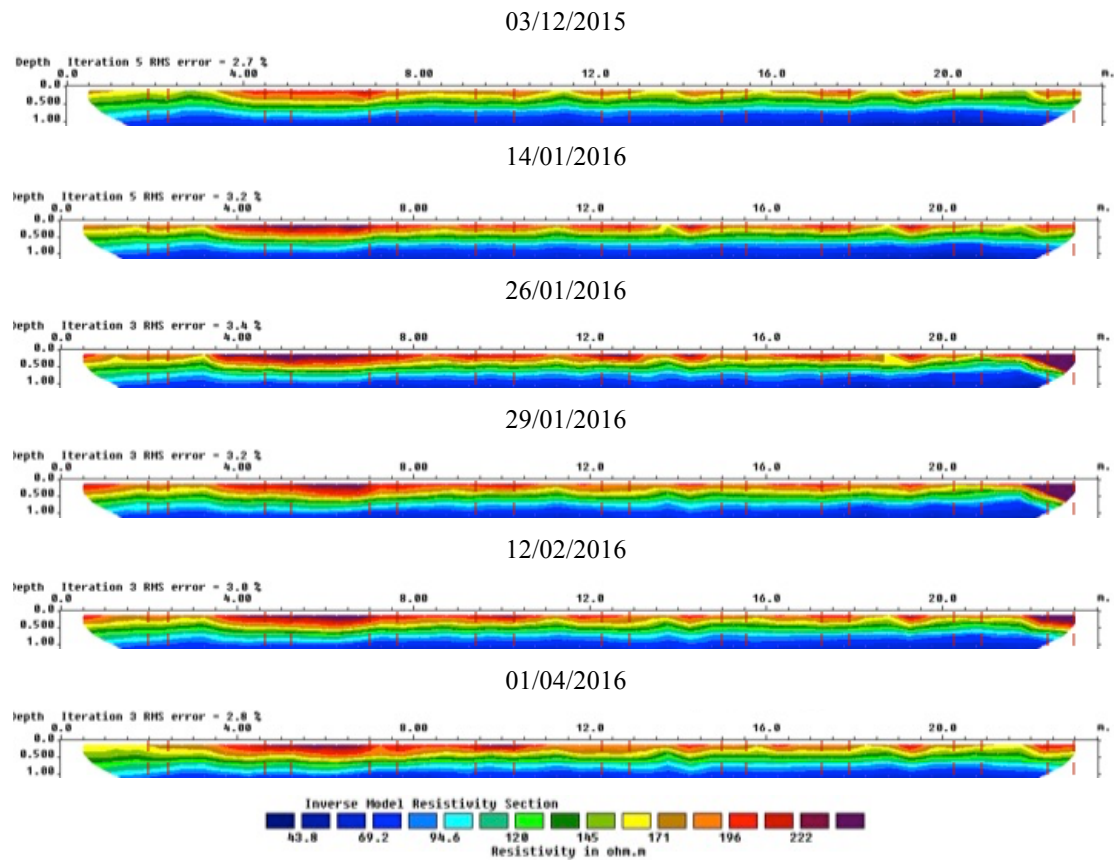


Figure 5-2: The resulting ERT images from the time-lapse measurements with results from 03/12/2015, 14/01/2016, 26/01/2016, 29/01/2016, 12/02/2016, and 01/04/2016. The colour codes of the resistivity values are displayed with the colour scale, which is given in Ωm . The stippled lines show positions of tire tracks.

The resistivity values are low around 0.7 to 1 meter depth in all of the images. This might indicate higher water contents below this depth, most likely saturated conditions, as the presence of water increases the soil's ability to conduct electricity (i.e. the inverse of resistivity) in these areas. Measurements of the groundwater table on 03/12/2015 indicate that the depth of the groundwater table varied between 0.5 and 0.7 meters across the profile, indicating saturated conditions below this depth similar to what the ERT image portrays. The top layer, i.e. the plough layer, has high resistivity values as the surface is red and the area just beneath is orange and yellow. This indicates that the soil in this area is more resistive, most likely due to unsaturated conditions. The resistivity values are particularly high in the southern end of the line, between 4 and 7 meters in the X direction, in all of the images. Such high values are also apparent on the northern tip of the line.

5.1.2 Temporal changes in resistivity

Images portraying changes have been generated to examine temporal variability in resistivity values across the profile. In Figure 5-3, each image illustrates percentage changes that have occurred from the previous data set, starting from 03/12/2015. See Table 5-1 for accumulated rainfall prior to each date. Positive percentage of resistivity corresponds to increased resistivity, while negative percentage of resistivity corresponds to more conductive (or most likely wetter) conditions.

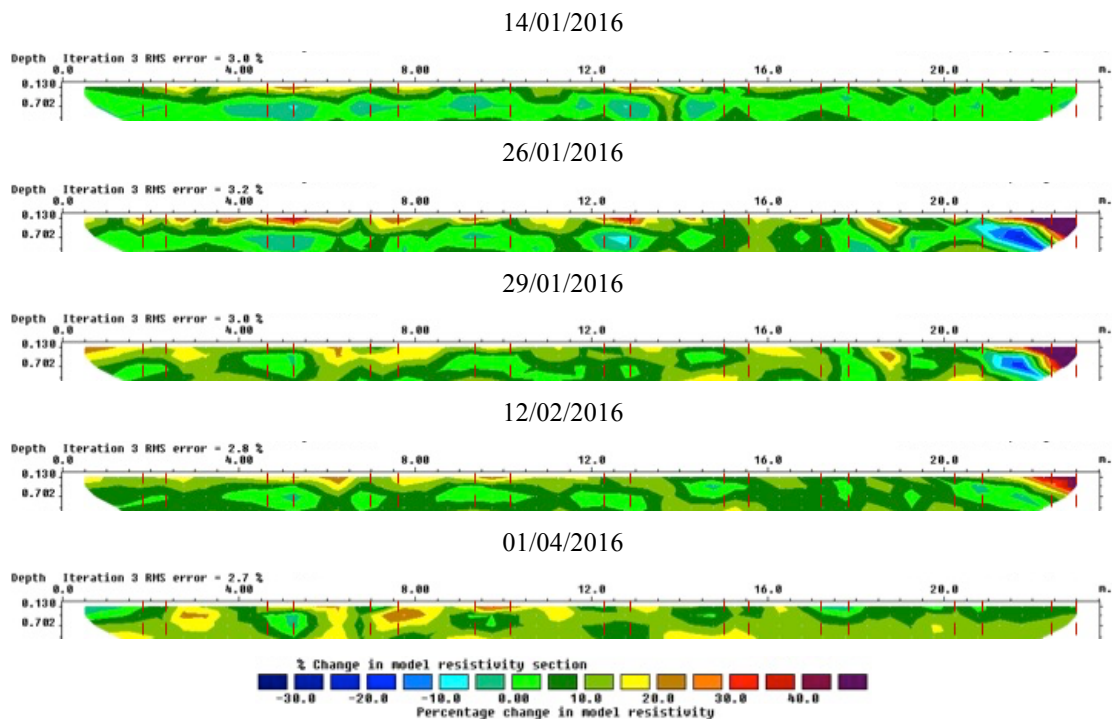


Figure 5-3: Percentage change in resistivity values from the previous measurement. Hence, 14/01/2016 shows the percentage change from 03/12/2015, 26/01/2016 from 14/01/2016, and so on. The stippled lines indicate positions of tire tracks.

The images illustrate a general positive change in resistivity values, which means that there was a decrease in the water content between the measurements. The greatest change occurred mostly in the topsoil, indicating that the resistivity values changed the most in the plough layer. In the image from 01/04/2016, though, this great positive change is also evident deeper in the profile. Except for the northern tip of the line, the resistivity values seemed to change the most in the southern part of the line. The northern tip might imply an anomaly as the resistivity in the topsoil increased greatly while the resistivity in the soil just beneath decreased greatly in the images from 26/01/2016, 29/01/2016, and 12/02/2016. The images

from 14/01/2016, 26/01/2016, 29/01/2016, and 12/02/2016 portray rather equal changes in resistivity values at around 0.8 meters depth, which indicate the occurrence of an agent affecting the water content. This depth coincides with the depth of the tile drains. In most of the images, the changes at this depth are positive, though in the image from 14/01/2016, there are patches at this depth with negative changes. Interestingly, these patches also coincide with the occurrence of tire tracks. This correlation is not as evident in the other images, however.

5.2 Infiltration

Double-ring infiltration tests express the rate of infiltration per area. In the field plot in Skuterud, the tire tracks appeared more compacted than the area between the tracks, which is consistent with the fact that vehicular activity is mainly confined to a controlled traffic pattern. Between the tracks, however, the soil did not appear to be affected by vehicular activity in the same way, as it seemed more porous. Hence, the rate of infiltration ought to differ when comparing the rates of the tracks and the area between the tracks. The tests were performed in order to estimate the saturated hydraulic conductivities of different parts of the field plot (see Figure 4-5), with the results given in Table 5-2. As the hydraulic gradient, i , is assumed to be 1, q is here equivalent to the saturated hydraulic conductivity, K_s . The state of the soil influences how capable the soil is to infiltrate water.

Table 5-2: The coordinates for each of the tests, indication for whether they were on or off a tire track, and the calculated rate of infiltration.

Test no.	X	Y	Tire track	q (m/s)
1	10	2		6.085E-05
2	11	2	x	1.324E-05
3	20	5		4.167E-05
4	21.5	5	x	2.294E-06
5	12	9		6.497E-05
6	13.5	9	x	7.645E-07

The resulting hydraulic conductivities were further used for statistical analysis, with the results given in Table 5-3. The infiltration tests performed on a tire track appeared to have lower infiltration rates than the ones performed between tracks, which indicates that the location of the tests did indeed affect the rate of infiltration. Based on these tests, the area that has not been subjected to compaction has on average a ten times higher ability to conduct water compared to the area that has.

Results

Table 5-3: Statistical analysis of the resulting hydraulic conductivities from the infiltration tests, including minimum and maximum values, mean, median, skew, standard deviation (σ), and variance (σ^2).

	Min	Max	Mean	Median	Skew	σ	σ^2
Track	7.645E-7	1.324E-5	5.432E-6	2.294E-6	1.634	6.804E-6	4.629E-11
No track	4.167E-5	6.5497E-5	5.583E-5	6.085E-5	-1.521	1.243E-5	1.546E-10

There appears to be a slight positive correlation (0.24) between the locations of the infiltration tests. A paired student t-test was also performed to test their correlation. The null hypothesis is that the average difference between the paired infiltration rates measured next to each other is zero. The resulting p-value is 0.02, which statistically means that the average difference between the paired infiltration tests is significantly different from zero, and the null hypothesis is, therefore, rejected.

5.3 Grain size distribution analysis

The grain size distribution analysis was performed on soil samples excavated from the entire field plot (see Figure 4-6). The grain size distribution analysis determined that all of the soil samples can be classified as silt loam, as is evident in Figure 5-4 and in the attached Excel file referred to in the Appendix. The silt content in each sample was around 60%, while the remaining 40% was almost equally divided between clay and sand. The decision concerning the material in the 2D vertical cross-sections created in HYDRUS was based on this analysis.

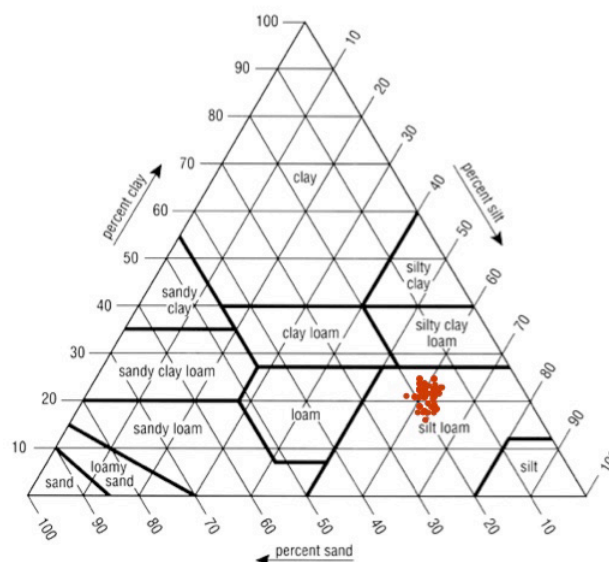


Figure 5-4: A modified version of the USDA (1993) soil triangle that includes the results from the sediment samples analysed.

The resulting values from the analysis were implemented in a statistical analysis, with the results given in Table 5-4 and in the kriged maps in a later section.

Table 5-4: Statistical analysis of the resulting distribution of grain sizes from the grain size distribution analysis, including minimum and maximum values, mean, median, skew, standard deviation (σ), and variance (σ^2) of clay, silt, and sand.

	Min	Max	Mean	Median	Skew	σ	σ^2
Clay	16.300	23.800	21.090	21.400	-0.848	1.796	3.226
Silt	59.000	63.600	61.445	61.300	0.131	1.145	1.311
Sand	15.100	20.400	17.471	17.300	0.437	1.438	2.067

5.4 Water retention characteristics

The water retention characteristics analysis was performed on soil samples excavated from the entire field plot (see *Figure 4-3*). The resulting data is given in the attached Excel file referred to in the *Appendix*. Water retention curves were plotted with the volumetric water content at each suction level, which are given in *Figure 5-5*. They illustrate how the volumetric water content changes a lot at pF values greater than 2. There is also a rather great change at pF values below 0.8. Between these two pF values, however, the volumetric water content of each sample appears to be rather stable. The samples collected from tire tracks appear to have among the lowest initial volumetric water contents, though they stabilize with among the highest volumetric water contents of all of the samples at pF values between 0.8 and 2.

Results

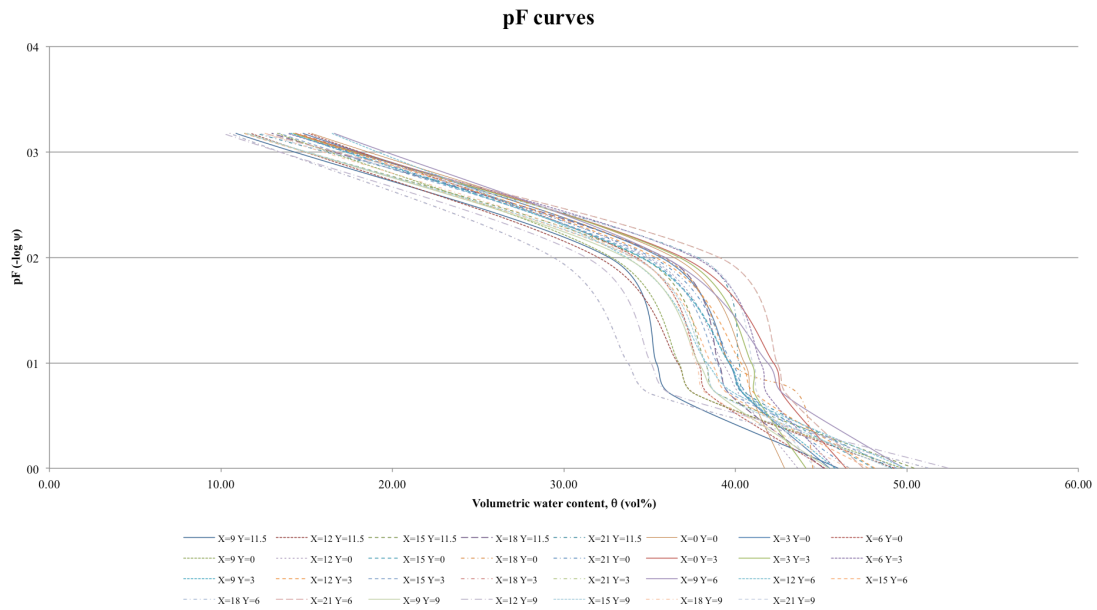


Figure 5-5: Water retention (pF) curves of the soil samples that were analysed for water retention characteristics portraying the volumetric water contents at different pF values.

The resulting values from the analysis were further used in a statistical analysis, with the results given in Table 5-5 and in the kriged maps in the next section.

Table 5-5: Statistical analysis, including minimum and maximum values, mean, median, skew, standard deviation (σ), and variance (σ^2), of the parameters from the water retention characteristics hydraulic conductivity, saturated and residual water content, air capacity, density, and porosity and the in-situ measurements of the water retention parameters water content, suction, and temperature.

		Min	Max	Mean	Median	Skew	σ	σ^2
Water retention characteristics	Hydraulic conductivity	2.928E-3	4.879	0.695	0.292	2.722	1.167	1.361
	Saturated water content	38.592	53.065	44.027	43.299	0.754	3.470	12.040
	Residual water content	3.766E-5	3.038	0.114	1.073E-3	5.475	0.556	0.298
	Air capacity	2.850	22.401	10.445	9.870	0.379	4.548	20.685
	Density	1.134	1.452	1.313	1.310	0.026	0.075	0.006
	Porosity	43.620	56.131	49.447	49.785	-0.288	3.031	9.184
In-situ water retention parameters	Water content	0.164	0.290	0.244	0.247	-0.243	0.030	9.160E-4
	Suction	-9.600	-11.700	-10.531	-10.500	-0.268	0.447	0.200
	Temperature	8.402	17.025	9.771	9.417	1.190	2.241	5.021

By comparing specific parameters, it is possible to increase the understanding of the influence that topsoil compaction has on the physical properties of the soil. In Figure 5-6, hydraulic conductivity is plotted against density to illustrate their relationship. Whether the soil sample was extracted from a tire track or not is included to be able to determine whether, based on the water retention characteristics analysis, there is a correlation between where the sample was excavated and the hydraulic conductivity/density relationship. According to the diagram, all of the soil samples from tire tracks had very high densities, and three of them also had very small hydraulic conductivities. One anomaly exists as one sample from a track had a higher hydraulic conductivity than many of the soil samples excavated from between the tracks. The densities of the soil samples from the tracks are higher than most of the samples from between the tracks. Three samples from between the tracks have higher densities, however. These samples were excavated in a very close proximity to the tracks; it is plausible that these areas had also been affected by vehicular activity.

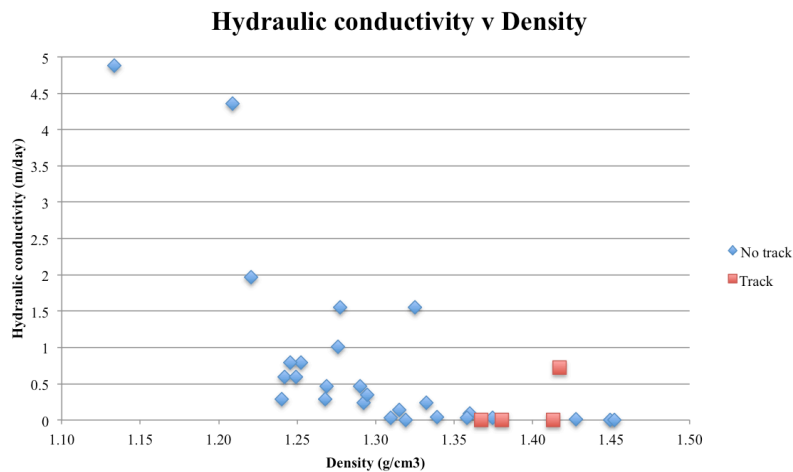


Figure 5-6: The relationship between the hydraulic conductivity and the density of the soil samples. The red squares represent soil samples excavated from tire tracks, while the blue diamonds represent soil samples excavated between tracks.

An individual statistical analysis was conducted on the samples excavated from tire tracks and the samples excavated between the tracks, which is given in Table 5-6. The focus of this analysis was to aid Figure 5-6 in increasing the understanding of how the parameters density and hydraulic conductivity might vary based on the location of excavation. The table shows how the densities of the samples from between tracks span across a larger range and that the minimum and maximum values are smaller and larger, respectively, compared to the samples

from the tire tracks. The area between the tracks has a much higher maximum value of hydraulic conductivity, but the variance appears to be a lot higher as well.

Table 5-6: Statistical analysis of the parameters density and hydraulic conductivity from the tire tracks and between the tire tracks, including minimum and maximum values, mean, median, skew, standard deviation (σ), and variance (σ^2).

		Min	Max	Mean	Median	Skew	σ	σ^2
Track	Density	1.367	1.417	1.395	1.397	-0.221	0.024	5.978E-4
	Hydraulic conductivity	2.928E-3	0.725	0.184	3.824E-3	2.000	0.361	0.130
No track	Density	1.134	1.452	1.301	1.292	0.297	0.073	5.325E-3
	Hydraulic conductivity	2.928E-3	4.879	0.771	0.292	2.540	1.228	1.509

Further, the resulting values were implemented in the creation of the computer models in HYDRUS. In Table 5-7 are the average values of soil density, pore volume, hydraulic conductivities, and the van Genuchten parameter n given, all of which have been implemented in the models' designs. The van Genuchten parameter α was neglected as the values retrieved from SWRC Fit were much smaller than the defaulted value for silt loam in HYDRUS and the range of values for that specific soil type provided by Ghanbarian-Alavijeh et al. (2010).

Table 5-7: The average values of soil density (ρ), porosity (n), and the hydraulic conductivities of compacted ($K_{s\ sub}$) and uncompactd (K_s) soil from the water retention characteristics analysis, as well as a van Genuchten parameter (n) produced by SWRC Fit with the results from the same analysis.

Water retention characteristics analysis				van Genuchten
ρ g/cm ³	n vol%	K_s m/day	$K_{s\ sub}$ m/day	n -
1.301	49.889	0.695	0.068	1.198

5.5 SGeMS

A statistical analysis has been performed based on the analysis of the soil samples, with the most interesting results being presented in this section. The remaining results are found in Appendix D.

Results

In Table 5-8 and Table 5-9, the calculated correlations between the values from the in-situ and laboratory measurements are provided, which have been implemented in the interpretation of the kriged maps.

Table 5-8: The calculated correlations between the in-situ measured water retention parameters water content, suction, and temperature.

	Water content	Suction	Temperature
Water content	1.00	0.06	-0.40
Suction	0.06	1.00	-0.12
Temperature	-0.40	-0.12	1.00

Results

Table 5-9: The calculated correlations between the grain sizes from the grain size distribution, clay, silt, and sand, and the parameters from the water retention characteristics analyses, hydraulic conductivity, saturated and residual water content, air capacity, density, porosity and the van Genuchten parameters n and α .

	Grain size distribution			Water retention characteristics and van Genuchten parameters								
	Clay	Silt	Sand	Hydraulic conductivity	Saturated water content	Residual water content	Air capacity	Density	Porosity	n	α	
Grain size distribution	Clay	1.00	-0.58	-0.69	0.16	0.09	0.07	0.30	-0.25	0.29	-0.06	0.00
	Silt	-0.58	1.00	-0.19	0.01	0.17	0.03	0.05	-0.07	0.03	-0.14	0.03
	Sand	-0.69	-0.19	1.00	-0.18	-0.22	-0.11	-0.39	0.34	-0.37	0.18	-0.01
Water retention characteristics and van Genuchten parameters	Hydraulic conductivity	0.16	0.01	-0.18	1.00	0.62	-0.08	0.76	-0.66	0.63	-0.24	0.75
	Saturated water content	0.09	0.17	-0.22	0.62	1.00	0.06	0.54	-0.58	0.58	-0.50	0.56
	Residual water content	0.07	0.03	-0.11	-0.08	0.06	1.00	0.01	-0.05	0.02	-0.19	0.08
	Air capacity	0.30	0.05	-0.39	0.76	0.54	0.01	1.00	-0.91	0.93	-0.36	0.61
	Density	-0.25	-0.07	0.34	-0.66	-0.58	-0.05	-0.91	1.00	-0.97	0.42	-0.55
	Porosity	0.29	0.03	-0.37	0.63	0.58	0.02	0.93	-0.97	1.00	-0.40	0.52
	n	-0.06	-0.14	0.18	-0.24	-0.50	-0.19	-0.36	0.42	-0.40	1.00	-0.51
	α	-3.00E-3	0.03	-0.01	0.75	0.56	0.08	0.61	-0.55	0.52	-0.51	1.00

5.5.1 Grain size distribution

In Figure 5-7, the omnidirectional variograms of the resulting grain size distribution analysis of the soil samples excavated from the field plot (see Figure 4-6 for the locations of the samples) are given, where A, B, and C illustrate the correlation of the clay, silt, and sand contents, respectively. According to the variograms, the data points are no longer correlated at distances greater than 11 meters for clay, 14.5 meters for silt, and 12.5 meters for sand. These variograms were further implemented to create kriged maps portraying the spatial variability of the grain sizes.

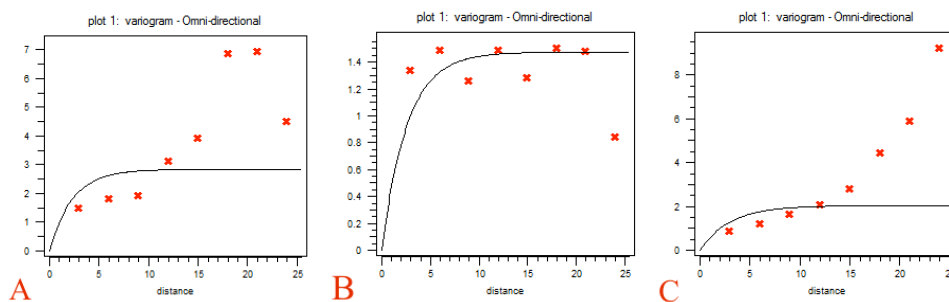


Figure 5-7: Omnidirectional variograms of clay (A), silt (B), and sand (C) from the grain size distribution analysis. Created in SGeMS.

In Figure 5-8 (and in Appendix D), the kriged maps of the grain sizes are presented, where A, B, and C represent the spatial variability of clay, silt, and sand, respectively. The images portray how the clay content is largest in the northern part of the field, the sand content is largest in the southern part of the field, and the silt content appears to be more random. According to Table 5-9, all of the grain sizes are negatively correlated to one another. Clay and sand appear rather highly negatively correlated (-0.69), while clay and silt appears a little less negatively correlated (-0.58). Silt and sand are the least negatively correlated (-0.19).

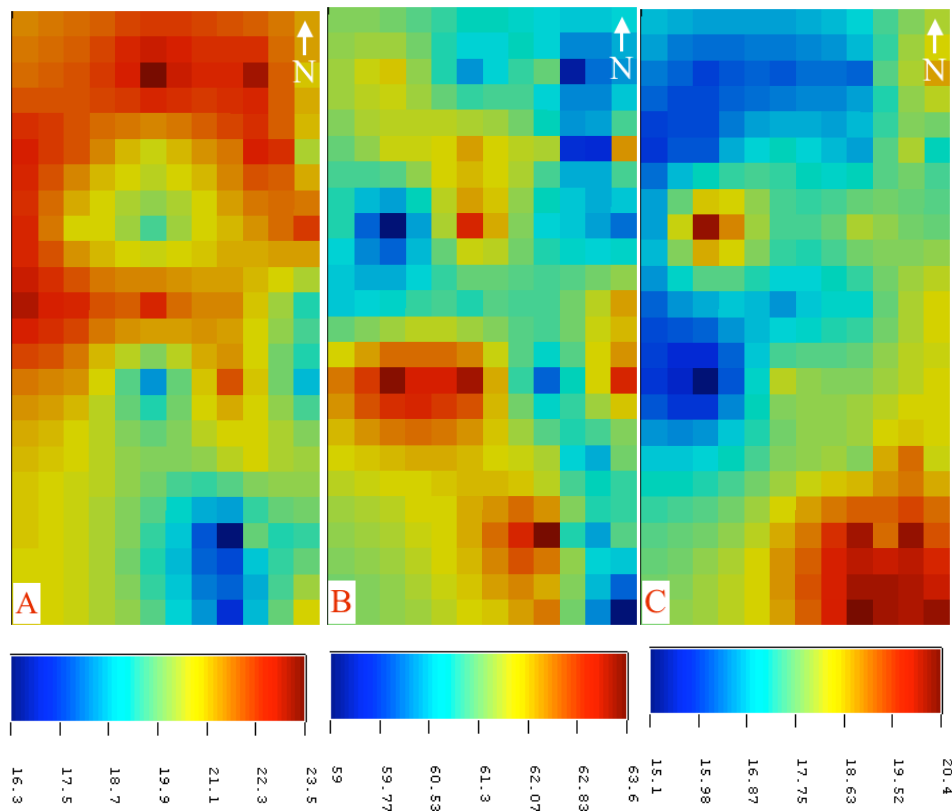


Figure 5-8: The kriged maps of clay (A), silt (B), and sand (C) from the grain size distribution analysis. The scales are given in %. Created in SGeMS.

5.5.2 Water retention characteristics

In Figure 5-9, the omnidirectional variograms of the resulting parameters from the water retention characteristics analysis of the soil samples excavated from the field plot (see Figure 4-6 for the locations of the samples) are given, where A-G represent the spatial variability of air capacity, air permeability, density, hydraulic conductivity, porosity, residual and saturated volumetric water content, and the van Genuchten parameters α and n , respectively. According to the variograms, the data points are no longer correlated at distances greater than 12 meters for air capacity, 13.5 meters for air permeability, 17 meters for density, 15.5 meters for hydraulic conductivity, 11 meters for porosity, 10 meters for residual volumetric water content, 17 meters for saturated volumetric water content, 12.5 meters for α , and 11 meters for n . These variograms were further implemented to create kriged maps portraying the spatial variability of the water retention characteristics.

Results

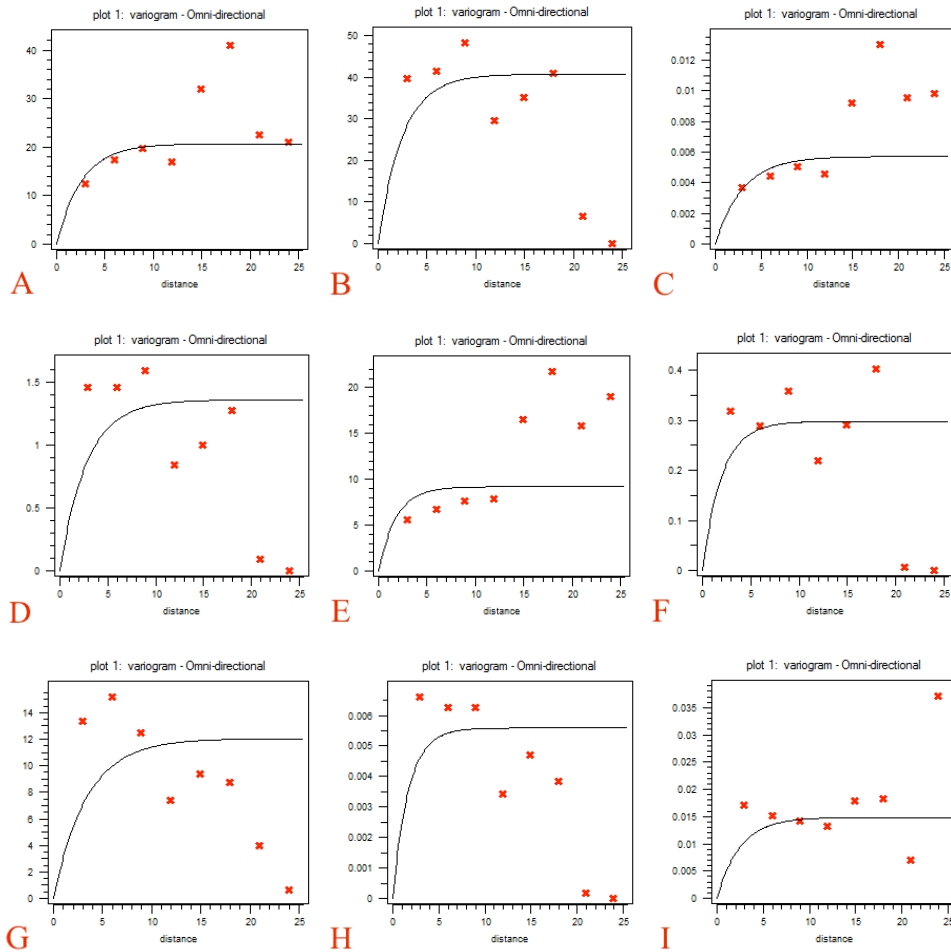
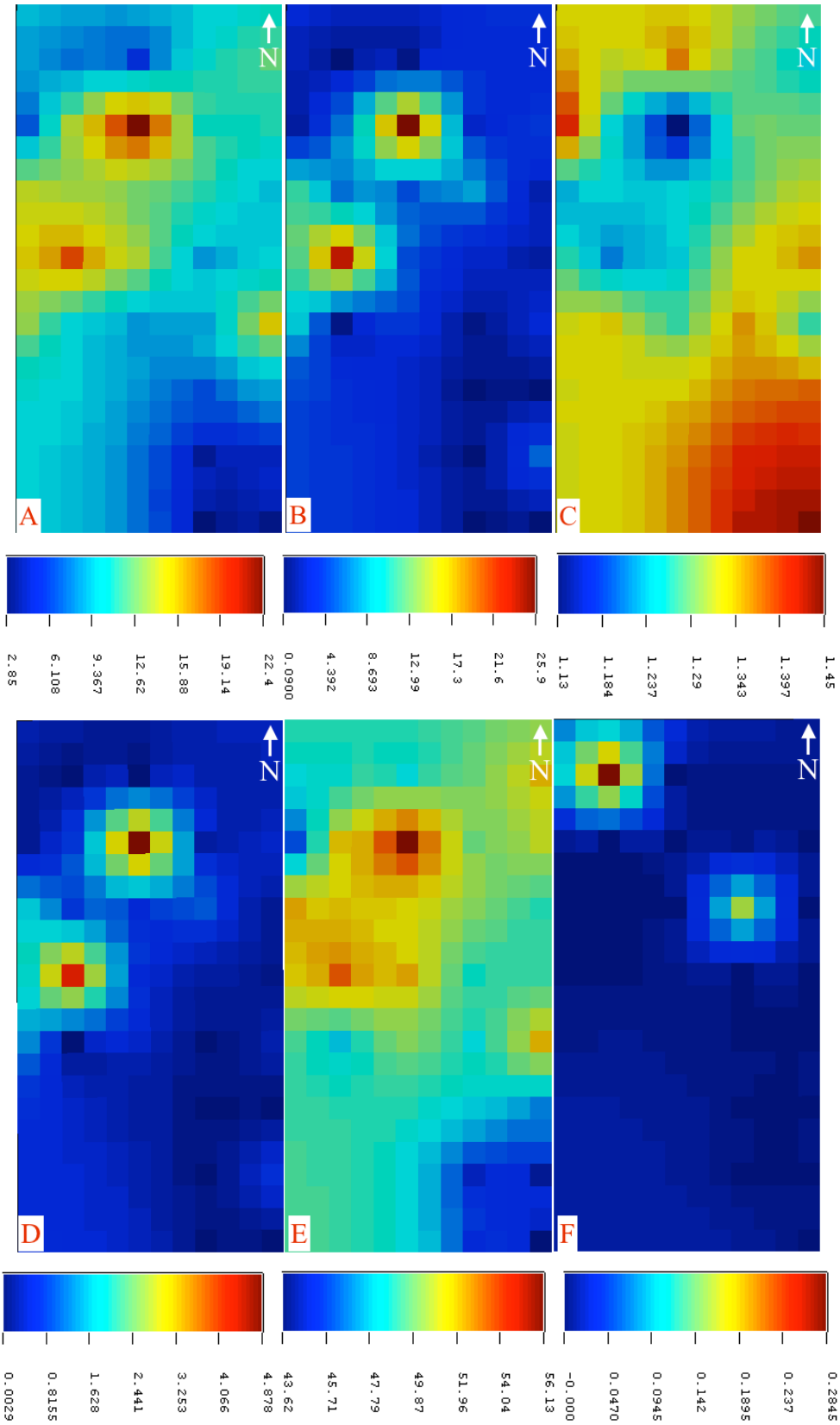


Figure 5-9: Omnidirectional variograms of air capacity (A), air permeability (B), density (C), hydraulic conductivity (D), porosity (E), residual volumetric water content (F), saturated volumetric water content (G), and the van Genuchten parameters α (H) and n (I) from the water retention characteristics analysis. Created in SGeMS.

In Figure 5-10, the resulting kriged maps of the results from the water retention characteristics analysis are portrayed, where A-G represent the spatial variability of air capacity, air permeability, density, hydraulic conductivity, porosity, residual volumetric water content, saturated volumetric water content, and the van Genuchten parameters α and n , respectively. The Northwest and the Southeast areas in the field plot stand out in all of the kriged maps, with either very high or very low values. According to Table 5-9, there is a very strong positive correlation between the parameters porosity and air capacity (0.93), which is evident by their similar kriged maps. These parameters are also rather highly positively correlated to hydraulic conductivity, and a little less positively correlated to α and saturated volumetric water content. It is also evident that density is strongly negatively

correlated to porosity and air capacity, and a little less negatively correlated to hydraulic conductivity, saturated volumetric water content, and α . These negative correlations are evident when examining the kriged maps of the parameters in question. The areas with e.g. high porosity and hydraulic conductivity are simultaneously the areas where the soil matrix has the lowest density. In the densification of a soil matrix, the pores might be compressed to smaller sizes and the network of interconnected pores might decrease. This will consequently decrease the ease of fluid to pass through the soil matrix as the matrix forces increase with decreasing pore size. The van Genuchten parameter n and the grain size sand are the only parameters that appear to be positively correlated to density.

Results



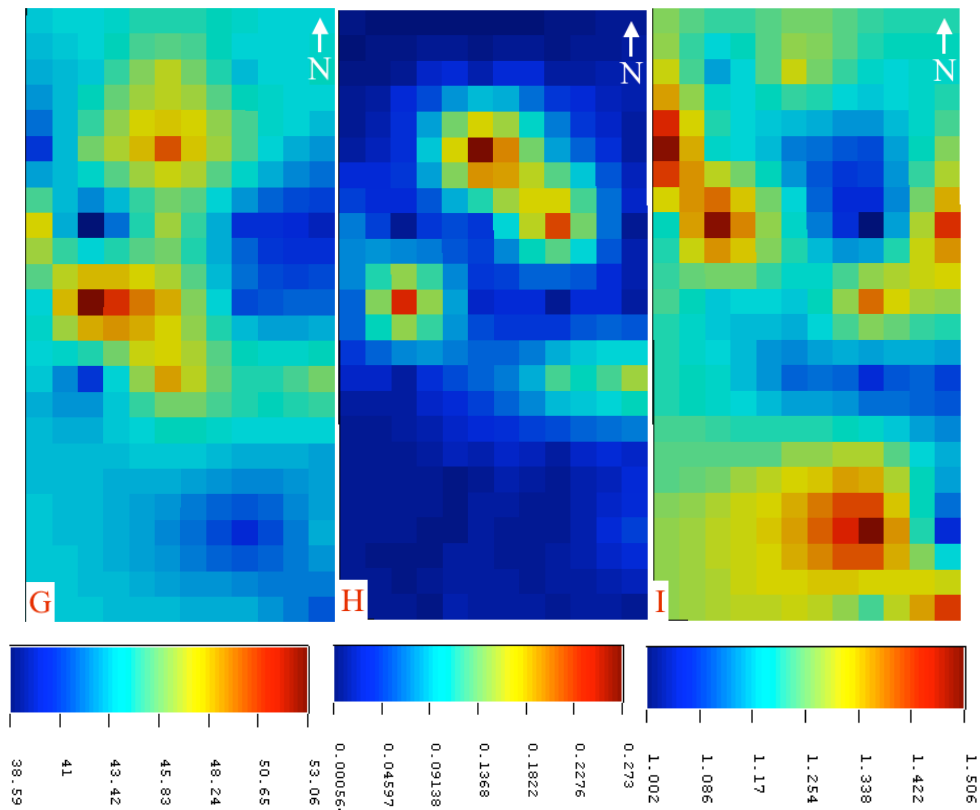


Figure 5-10: The kriged maps of air capacity in vol% (A), air permeability in μm^2 (B), density in g/cm^3 (C), hydraulic conductivity in m/day (D), porosity in vol% (E), residual volumetric water content in vol% (F), saturated volumetric water content in vol% (G), the van Genuchten parameter α in $1/\text{m}$ (H) and the dimensionless van Genuchten parameter n from the water retention characteristics analysis. Created in SGeMS.

The residual volumetric water content is the parameters that appears the least correlated to all of the other parameters, which is evident both in Table 5-9 and when comparing the kriged maps of the parameters. A possible explanation might be that there exists error values that are so high that they affect the dispersion of colour of the lower values, and, hence, the entire map.

5.5.3 In-situ water retention parameters

In Figure 5-11, the omnidirectional variograms of the water retention parameters from the in-situ measurements (see Figure 4-3 for the locations of the measurements) are given, with referral to the Excel file with the data in the Appendix. A, B, and C represent suction, temperature, and volumetric water content, respectively. According to the variograms, the data points are no longer correlated at distances greater than 16 meters for suction, 12 meters

for temperature, and 17 meters for volumetric water content. These variograms were further implemented to create kriged maps portraying the spatial variability of the water retention characteristics measured in the field.

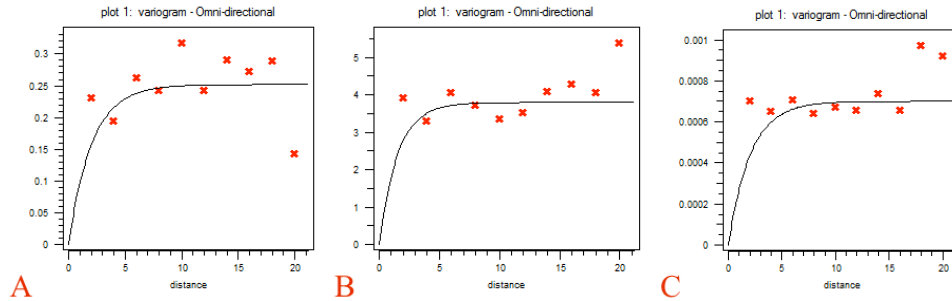


Figure 5-11: Omnidirectional variograms of suction (A), temperature (B), and volumetric water content (C) from the in-situ measurements of water retention parameters. Created in SGeMS.

In Figure 5-12, the resulting kriged maps of the results from the in-situ measurements of water retention characteristics are given, where A, B, and C represent the spatial variability of suction, temperature, and volumetric water content, respectively. According to Table 5-9, suction and volumetric water content is not correlated to a great extent (0.06), though suction seems to be more strongly negatively correlated to the temperature that exists in the ground (-0.40).

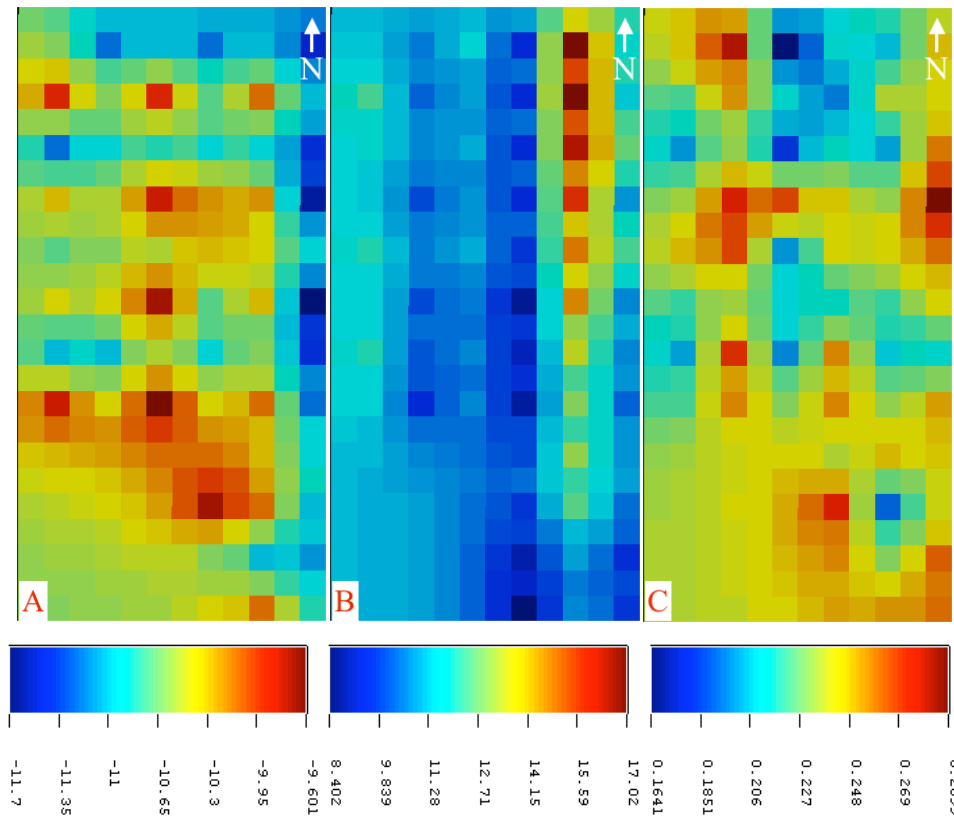


Figure 5-12: The kriged maps of suction in kPa (A), temperature in °C (B), and volumetric water content in m^3/m^3 (C) from the in-situ measurements of water retention characteristics. Created in SGeMS.

The kriged maps of suction and temperature portray a streaky pattern in the north-south direction. Directional variograms reveal that the range of correlation is dependent upon the direction. In Figure 5-13, the directional variograms of temperature in the 0° and 45° angles are given, which demonstrate how the points are no longer correlated after 8 meters in the 0° angle and after 10 meters in the 45° angle. It is possible that by using different distances of range, the difference of correlation distances between the angles is even more evident.

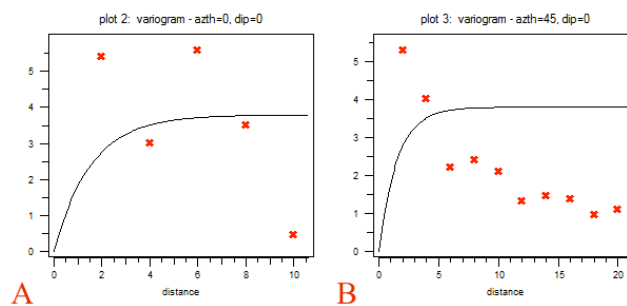


Figure 5-13: Directional variograms of temperature portraying the range of correlation in the 0° and 45° angles. Created in SGeMS.

5.6 HYDRUS

The 2D vertical cross-sections simulated the resulting flow of the precipitation periods of M1, M2, and M3. In Figure 5-14, the precipitation of the three scenarios is cumulatively illustrated, and variations in the precipitation patterns exist when comparing them. In both M1 and M2, the total amount of precipitated water was close to equal. However, there was a large difference in the patterns of precipitation. In M1, precipitated water came primarily during the first seven days, while, in M2, the precipitation periods were more evenly spread out throughout the month. M3 stands out, as the total precipitated water equals almost twice the amount as in the other months. Also in this month, precipitation periods were rather evenly spread out, though with more rapidly occurring intervals and with a higher incoming flux than in M2.

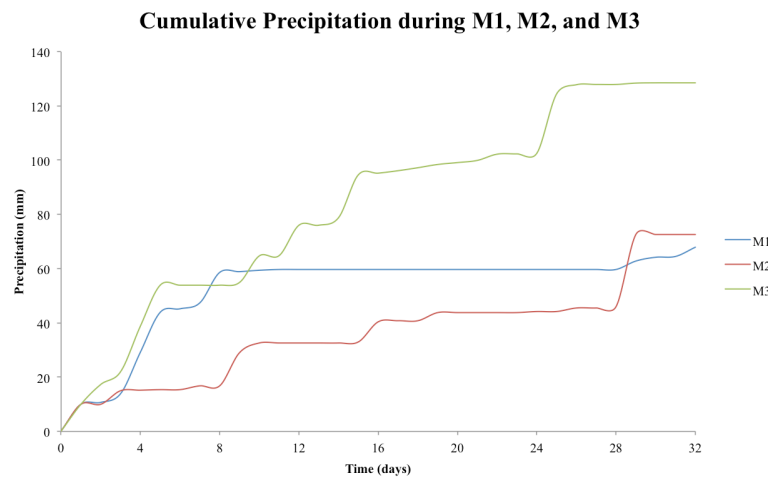


Figure 5-14: The cumulative precipitation during M1, M2, and M3 used to define the top boundary flux in the HYDRUS models.

In the following subsections, the movement of water during the three months is examined in a 2D view.

5.6.1 Simulations of flow and the impact of compaction

Simulating flow of water through the two cross-sections illustrated how water moves vertically through the soil matrix. By simulating the resulting flow of three distinct precipitation patterns, it is plausible to gain an understanding of the flow and to discuss potential affecting factors. The breakthrough curves of the three scenarios M1, M2, and M3

(extended to 60 days) in Cross-Section 1 and Cross-Section 2 is displayed in Figure 5-15. The curves portray the cumulated concentrations of the tracer plume that reached the tile drain. In Table 5-10, the retention time, i.e. the time before half of the concentration had reached the tile drain, of the tracer in each of the scenarios in both of the cross-sections is given.

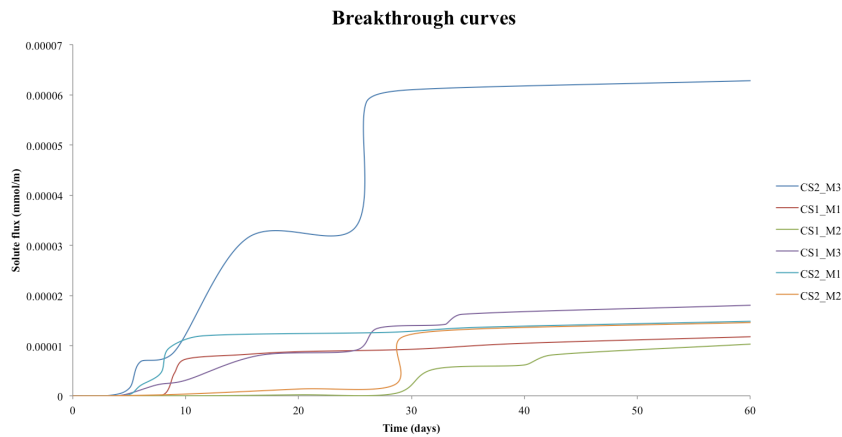


Figure 5-15: The breakthrough curves of the three scenarios M1, M2, and M3 extended to 60 days in the two models Cross-Section 1 and Cross-Section 2 (CS1 and CS2, respectively).

Table 5-10: The retention time of the scenarios M1, M2, and M3 in both of the cross-sections and the precipitating water in millimetres during this period of time.

	Cross-sections					
	CS1: Subsoil compaction			CS2: No subsoil compaction		
	No. of days	C/C ₀	Precipitation (mm)	No. of days	C/C ₀	Precipitation (mm)
M1	9.6	6.05E-6	59.18	8.1	6.94E-6	58.64
M2	30.9	3.82E-6	72.60	28.7	5.40E-6	63.90
M3	19.8	8.44E-6	98.97	14.1	2.64E-5	79.61

Examining the two cross-sections separately reveals that the pattern of precipitation affects the rate of flow. M1 was the scenario with the most precipitation in the beginning, which resulted in a rapid movement of the tracer in both of the cross-sections. The tracer moved at the lowest rate during M2, which is likely due to the small and spread out precipitation periods. Within the first five days, the tracer moved at the fastest rate of all the scenarios in M3 in Cross-Section 2, which also represents the scenario and the cross-section with the highest total concentration that reached the tile drain. This is evident in both Figure 5-15 and Table 5-10.

Comparisons of Cross-Section 1 and Cross-Section 2 indicate to what degree subsoil compaction might affect the flow. During all of the scenarios, the tracer moved at a higher rate in Cross-Section 2 than in Cross-Section 1, which indicates that subsoil compaction decreased the overall flow rate. In Figure 5-16, the spreading of the tracer on M2:11 in both of the cross-sections is portrayed. The influence that compaction has on the flow is easy to comprehend from these two images: where there is no subsoil compaction, the rate of flow is much higher.

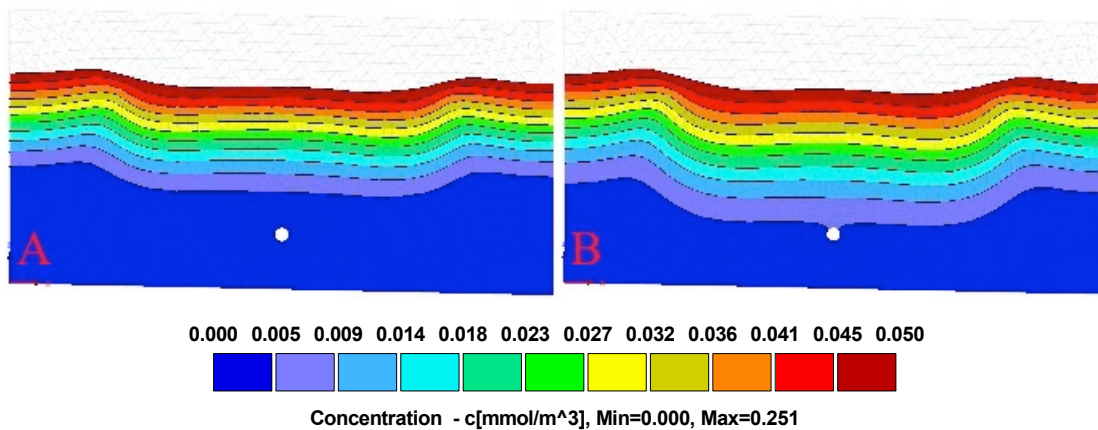


Figure 5-16: The colour scale and spreading of the tracer on M2:11, in Cross-Section 1 (A) and Cross-Section 2 (B). The cross-sections are both grey at the top as the concentration of the tracer is not within the scaling range. Created in HYDRUS 2.04.

The occurrence of topsoil compaction is easy to notice in both images in Figure 5-16. The velocity of flow was higher between the tire tracks, which resulted in a greater longitudinal dispersion in this area than within the tracks.

5.6.2 Changes in velocity

Where compaction has occurred, the pores have been compressed to smaller sizes, making some of them unavailable for flow. This might lead to a decrease in the flow velocity, which is well illustrated in Figure 5-17 and Figure 5-18 where the velocity isolines and vectors are given for the flow on M1:5 in Cross-Section 1 and Cross-Section 2, respectively. It is evident that the flow in the area between the tire tracks, which has not been subjected to topsoil compaction, moved at a higher rate compared to the flow of water within the tracks. What is interesting is that the water that was already flowing in this *corridor* of uncompacted soil was flowing vertically, while parts of the flow in the tracks were flowing at an angle towards

the less compacted area. The red arrows are depicting this occurrence. Where the water from the tire tracks met the water between the tracks, the velocity of flow appeared to increase. Once the flow reached layer number two, parts of the flow changed direction and headed for the corners before straightening up. The rest of the flow continued vertically towards the base of the cross-sections due to the homogeneity of the sub-layer. There is a clear difference in the velocities of the sub-layers between the two cross-sections; even though the flow appears to follow equal patterns, the rates of flow differ greatly. Hence, topsoil compaction appears to have an impact on the direction of flow, while compaction in general affects the velocity of flow.

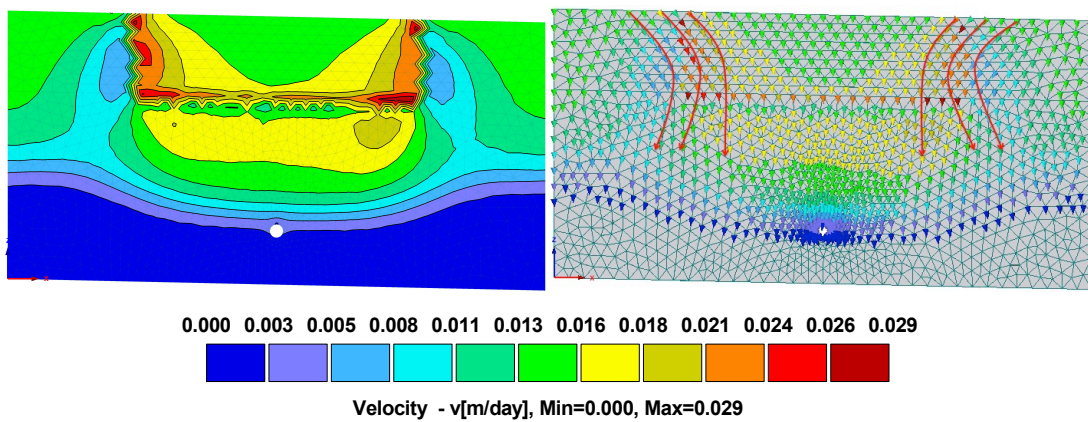


Figure 5-17: The change of velocity on M1:5 in Cross-Section 1 is portrayed isolines and velocity vectors, where the vectors depict the direction of flow. The red arrows are included to accentuate this. The colour scale is also provided. Created in HYDRUS 2.04.

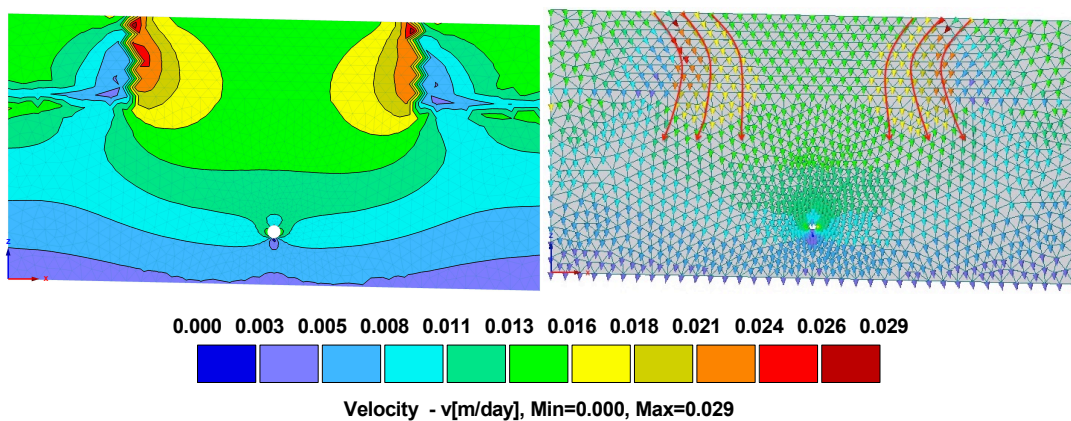


Figure 5-18: The change of velocity on M1:5 in Cross-Section 2 is portrayed with isolines and velocity vectors, where the vectors depict the direction of flow. The red arrows are included to accentuate this. The colour scale is also provided. Created in HYDRUS 2.04.

5.6.3 Drainage efficiency

Both cross-sections include tile drains with the purpose of removing the incoming flux. In Table 5-11, the drainage efficiency, i.e. the ratio between the volume drained through the internal sinks and the rainfall volume (Aronica and Lanza 2005), of the tile drain in each cross-section during M1, M2, and M3 is given. The tile drain had increased efficiency of removal of water where there was no subsoil compaction present, as Cross-Section 2 had higher drainage efficiency during all three scenarios. It is also evident that both the amount and pattern of incoming flux affected the efficiency of the tile drain. M3 was the period with the highest total flux, and it also had the highest drainage efficiency. Even though M2 had a higher incoming flux than M1, the tile drain had higher removal efficiency during M1. It is possible that the pattern of precipitation caused this, and that the spread out precipitation periods during M2 decreased the efficiency of the tile drain. It is also plausible that the location of the tile drain relative to the tire tracks affected the drainage efficiency in the two cross-sections.

Table 5-11: The drainage efficiency of the tile drain in Cross-Section 1 and Cross-Section 2 during M1, M2, and M3.

	Cross-Sections					
	CS1: Subsoil compaction			CS2: No subsoil compaction		
	Total Flux m ²	Drained flux m ²	Drainage efficiency %	Total Flux m ²	Drained flux m ²	Drainage efficiency %
M1	0.136	0.050	36.451	0.136	0.081	59.647
M2	0.145	0.028	19.284	0.145	0.067	46.143
M3	0.257	0.145	56.420	0.257	0.220	85.603

5.6.4 Dispersion of tracer plumes

When compaction affects the pores to the extent that they become unavailable for flow, the preferred flow ways change and the tortuosity increases. Tracers were added to three locations in the topsoil in Cross-Section 2 with the intention of examining the spreading of each plume and, hence, the flow of water. The two plumes on the sides had its source in tire tracks where the soil is compacted, while the plume in the middle had its source between the tracks where there is no compaction. When observing the spreading of the three plumes, it is evident that the middle one was spreading mainly vertically towards the tile drain, while the

two on the sides were spreading downward at an angle towards the middle. This was perhaps due to the tile drain absorbing fluid during saturated conditions, which led the water to take different flow path than it would have without it present. The plumes on the sides seemed to diffuse rather similarly in the beginning. On M3:19 however, the left and middle plumes connected, while the right plume never, over the given time period, connected to the other plumes. The skewing of the model might be part of the reason for this outcome.

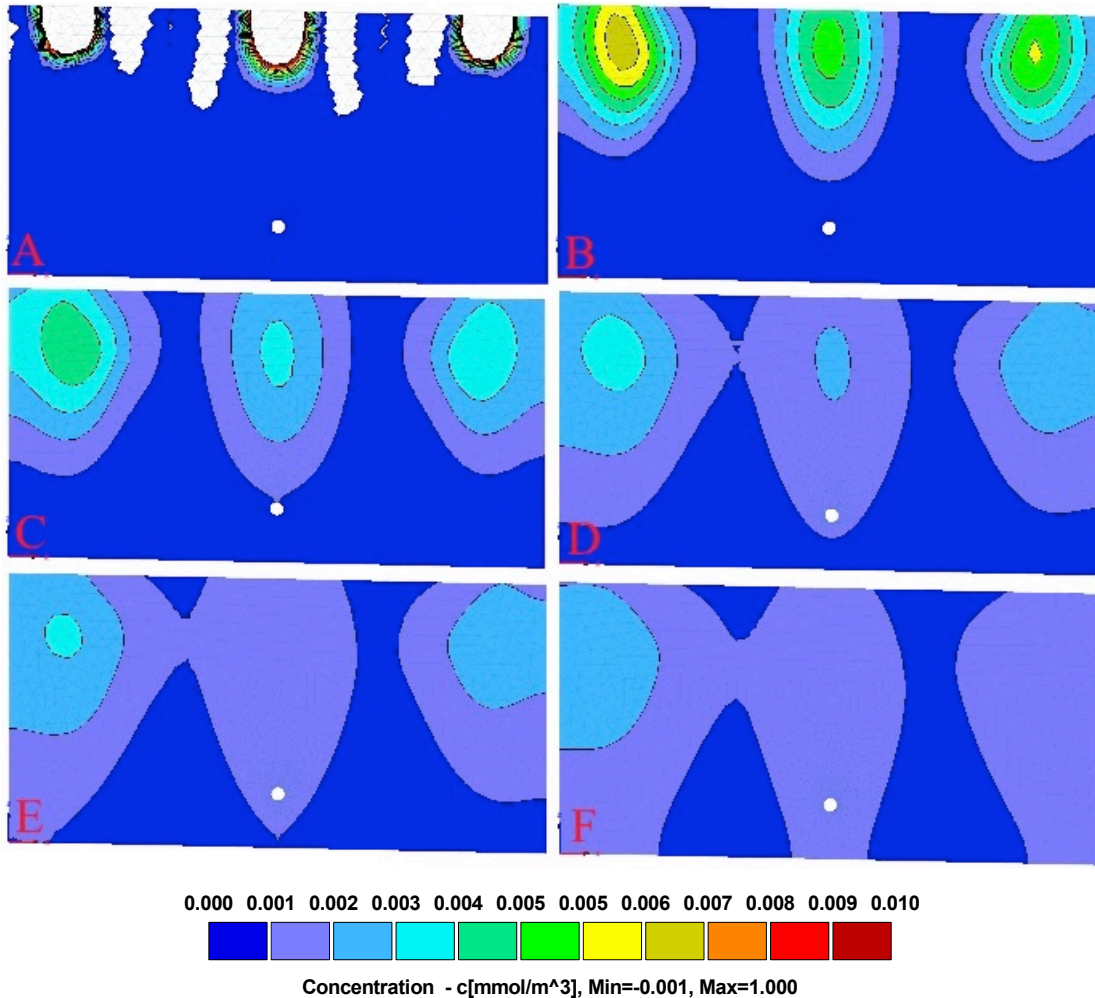


Figure 5-19: The scale and the spreading of the three tracer plumes in Cross-Section 2, where A-F represent M3:2, M3:5, M3:12, M3:19, M3:23, and M3:31, respectively. The grey areas represent where the concentration is higher than the given scale. Created in HYDRUS 2.04.

6 Discussion

6.1 *Physical measurements*

6.1.1 Temporal changes in resistivity

The electrical conductance of the soil highly depends on the concentration of ions in the pore water. The soil matrix gets more conductive as the ion concentration increases. If assuming that the ion concentration is constant, the electrical conductance of the matrix depends on the water content in the pores, and changes in the water content reflects the soil's ability to conduct an electrical current (Samouëlian et al. 2005). As the water content increases in the soil matrix, the electrical resistivity decreases as a consequence. When the water content of the pores are below 15%, an increase in water content gives a rapid decrease in resistivity (Samouëlian et al. 2005). When measuring the resistivity over time, the results reflect the climatic variations; if a rain event occurs, the resistivity decreases in the area of the soil matrix due to increased infiltration. The time-lapse ERT measurements obtained for this thesis contradict the expected change in resistivity values. Generally, the resistivity values increased between each of the measurements, even though it was during a period of melting snowpack. There are several theories that might explain this circumstance, though determining the actual cause of events persists to be challenging.

The image from 14/01/2016 in Figure 5-3 is portraying the percentage change in resistivity since 03/12/2016. It is evident that the resistivity values have increased across most of the profile, even though there was 25.3 mm of precipitation beforehand. As this was in the middle of January, 14/01/2016 also represents the time with the lowest temperature. Electrical resistivity decreases with increasing temperature as a consequence of increasing ion agitation as the fluid viscosity decreases (Samouëlian et al. 2005). Soil temperature measurements in that part of the Skuterud catchment area performed by the Nibio PhD student Torsten Starkloff reveal that the temperature had decreased from 1.4 °C on 03/12/2015 to -0.1 °C on 14/01/2016 at 10 cm depth, which means that it is plausible that the increasing resistivity values could be the results of the decreasing soil temperature.

Between 14/01/2016 and 26/01/2016, the temperature increased by 19.2 °C, though no infiltration had yet occurred. The resistivity values were hence expected to remain equal. According to the image from 26/01/2016 in Figure 5-3, the resistivity values increased across most of the profile, except for a few areas around 0.8 meters depth. Torsten Starkloff reports that the soil temperatures slightly decreased at different depths in the soil matrix from 14/01/2016 to 26/01/2016. Hence, as with the image depicting the change in resistivity from 03/12/2016 to 14/01/2016, it is possible that the fluid viscosity decreased and that the matrix increased its ability to resist conducting electrical currents.

Between 26/01/2016 and 29/01/2016, 17 mm of melted snowpack infiltrated into the ground, which would have reached a total of 17 cm if moving at a steady pace. However, the image portraying the change in resistivity values indicates increasing values across the profile. He et al. (2015) state that, due to ice lenses, ice-filled pores, or basal ice layers on the soil surface, the soil infiltration capacity might be inhibited and snowmelt may become runoff. One of the many factors affecting the infiltration capacity of the soil is the freeze-thaw cycle of the soil matrix, and the depth of the frost is highly controlled by the soil moisture content prior to freezing and the timing of snow accumulation on the ground; the frost depth might reach deeper than 0.5 meters into the ground if the freezing of the soil start before the accumulation of snow cover on the ground (He et al. 2015). However, there was no evident sign of runoff at the field plot to support this theory. Additionally, it does not suggest why the resistivity values increased between the measurements as the soil temperatures of the soil matrix remained stable. This might indicate that infiltration did in fact occur, but that the infiltrating water did not move evenly downward through the soil matrix. Preferential flow paths might be part of the answer: the flow might have occurred mainly through macro-pores in the soil matrix, which have the potential of conducting large amounts of water (Olsen 1998). Consequently, the high conducting macro-pores might have caused a fast generation of water through the soil matrix, which could potentially be the answer to why the resistivity values of the topsoil increased between the measurements. This is a matter that ought to be investigated more.

The images portraying percentage change in resistivity values also raise the question concerning the occurrence of decreased resistivity values at approximately 0.8 meters depth. Especially in the images resulting from the measurements on 14/01/2016 and 26/01/2016,

there are several areas at this depth where the resistivity values have decreased rather than increased like in the rest of the profile. Interestingly, this depth coincides with the depth of the tile drains in the field. The patches appear to be dispersed horizontally, which might indicate ponding around the drains. The drains are implemented diagonally across the field plot (see Figure 2-4) with a spacing of 8-10 meters, which means that the patches of decreased resistivity values might be spaced too close together. There exists an old drainage system beneath the field plot, however, and it is plausible that a combination of the old and new systems caused of what is seen at 0.8 meters depth. Another interesting aspect regarding the patchy dispersion of the decreased resistivity values is that their occurrence somewhat coincides with the tire tracks. As demonstrated through the double-ring infiltration tests, the tire tracks have a lower saturated hydraulic conductivity compared to the area between the tracks. Perhaps the water that infiltrated prior to the measurement on 14/01/2016 moved at a slower rate in the tire tracks, resulting in their occurrence at 0.8 meters depth at the time of the measurement. A third explanation would be that the patches of decreased resistivity values at 0.8 meters depth appeared as a result of a combination of the tire tracks and the tile drains. However, further research is needed in order to resolve this matter.

6.1.2 Determining the existence of compaction

To determine whether compaction has taken place, there are several parameters that can be examined. Relative bulk density, for instance, provides directly comparable values for all types of soil. In Figure 5-6, the measured density of the soil samples is plotted against the calculated hydraulic conductivity. The general relationship between the two parameters is quite evident: the higher the hydraulic conductivity, the lower the density of the soil matrix. The figure implies that the increasing densities in the tracks lead to decreasing hydraulic conductivities. There are three samples with higher densities than the ones excavated from tire tracks. These were all excavated in close proximity to a track, and it is, based on these results, possible that these areas also has been affected by vehicular activity. As merely a few samples were collected from the tire tracks, however, it is plausible that they represent anomalies. Hence, it is advisable to collect and analyse additional soil samples from the tracks to support these findings. The statistical analysis of density and hydraulic conductivity in Table 5-6 show that, for the tire tracks, the density mean and median are larger and the hydraulic conductivity mean and median are smaller in the tire tracks than between the tracks. The values appear to vary more in the samples excavated from between the tracks, but

this might be merely because the sample population is a lot greater. Hence, additional samples from the tire tracks will increase the authenticity of the statistical analysis as well.

Compaction might affect the water retention of the soil due to the increasing density. Generally, the water retention increases at very low pF values, while, at higher pF values, the water content decreases with increasing compaction (Smith et al. 2001). The water retention (pF) curves plotted in Figure 5-5 portray draining of the soil samples during the water retention characteristics analysis. There appears to be a difference between the samples excavated from the tire tracks and the samples excavated between the tracks. The samples from the tracks appear to have among the lowest volumetric water contents at the beginning of the analysis, ranging from approximately 44 to 46 vol%. The highest volumetric water contents at more than 50 vol% originated from samples excavated in the middle between two tracks. When suction was subjected to the samples, the samples with the highest volumetric water contents appeared to drain the most before the water content stabilized, while the samples from the tire tracks were among the samples that appeared to drain the least. At the lowest pF values, it is mainly the largest pores that drain, as more suction is needed to be able to drain the smaller pores. In the densification of a soil matrix, the pores might be compressed to smaller sizes, which means that the number of macro-pores decreases (Mossadeghi-Björklund et al. 2016). Hence, a higher suction is needed to remove the same vol% of water from the pores in a compacted soil. This indicates that the samples from the tire tracks had a smaller number of large pores that could drain at small pF values, and that they consequently retained their water content longer than most of the samples excavated between the tracks. This supports the theory that the soil in the tracks is more compacted than the soil between the tracks.

To increase the understanding of the impact that compaction might have on the flow of water, soil water infiltration in the topsoil has been monitored to determine the compaction status of the surface area of the field plot. Compaction might indeed cause a large difference in the infiltration rate between compacted and uncompacted soil as water tends to infiltrate uncompacted soils with well-aggregated particles more rapid than massive, structure-less soils (Hamza and Anderson 2005). Based on the correlation analysis of the parameters (see Table 5-9) and the comparison of the kriged map of density and the kriged maps of air capacity, air permeability, and hydraulic conductivity (see Figure 5-10), it is indeed evident

that the areas with the highest densities also represent the areas that can hold the least air and have the lowest ability to transmit both air and fluids. Hence, this indicates that compaction does indeed influence the soil's ability to infiltrate water in the negative manner, which may cause surface runoff and erosion. Hamza and Anderson (2002) propose that compaction of the soil decreases the rate of infiltration, which the double-ring infiltration tests demonstrated. The tests, performed both on and between tire tracks, indicate that the areas that have been subjected to the most vehicular activity have a ten times lower saturated infiltration rate compared to the areas between the tracks. However, the difference between compacted and uncompacted soil is most evident at low moisture contents, as stated by Silva et al. (2000). At high moisture contents, the difference in soil resistance tends to be low; usually lower than the value that limits root growth, which is >2 MPa (Silva et al. 2000). Hence, the difference in infiltration rates will be even higher during unsaturated conditions compared to the saturated rates that were estimated here.

6.2 *Simulations*

The breakthrough curves in Figure 5-15 portray how the peak concentration during M3 in Cross-Section 2 was much greater than for the other scenarios in both of the cross-sections. This indicates that subsoil compaction and the amount/pattern of precipitation combined affects how much of the tracer that reaches the tile drain. As Cross-Section 2 does not have subsoil compaction, water is able to move more freely both vertically and horizontally, which was portrayed in M3, but not as clearly in M1 and M2. As displayed in Figure 5-14, however, the incoming precipitation during M3 was almost twice as high as during M1 and M2. It is plausible that, where there is no subsoil compaction, the rate of the tracer is highly dependent upon the flux, while, in profiles where there is subsoil compaction, the flux does not influence the movement of the tracer to the same degree.

It is important to recollect that there was only one characteristic that separated Cross-Section 1 from Cross-Section 2: the decreased saturated hydraulic conductivity of the subsoil. If the compacted areas had also had increased density, which would have increased the authenticity of the cross-sections, the outcome of the simulations might have been somewhat different. Decreasing pore sizes as a result of densification of the soil not only reduces the infiltration capacity of the medium, but also the storage capacity. Simultaneously, the risk of flooding and erosion increases, which also increases the risk of polluting surface waters with soil,

nutrients, and chemicals from the agricultural practice (Akker et al. 2003). It is plausible that with increased density of the compacted areas, the simulations might have generated similar situations.

6.2.1 Topsoil and subsoil compaction and its influence on drainage efficiency

Compaction of the soil profile in agricultural fields can generally be divided into the two groups topsoil compaction and subsoil compaction. Research has supported the theory that compaction of the topsoil is related to ground pressure, while compaction of the subsoil is related to total axle load independently of ground pressure (Hamza and Anderson 2005). Serious problems to crop growth and yield can be generated as consequences of reduction in water infiltration rate and root growth and development due to topsoil compaction (Mouazen et al. 2003). As topsoil compaction is related to ground pressure, the compaction occurs mainly directly beneath the tires of agricultural vehicles. The two cross-sections were designed with a controlled traffic pattern where the compaction was located in the tire tracks in the topsoil. When simulating the three scenarios in the two cross-sections, the velocity vectors (see Figure 5-17 and Figure 5-18) indicated how topsoil compaction might affect the flow as it is infiltrating into the ground. The vectors portrayed how water in the compacted soil seeks less dense areas and, consequently, flow at an angle towards the areas between the tracks. During periods of high incoming flux, there is a possibility that this might lead to ponding water on the surface and, consequently, surface runoff. However, topsoil compaction is not necessarily considered a permanent condition as it can be counteracted through the processes of freezing and thawing and actions such as ploughing. For farmers, a more severe problem exists in subsoil compaction. Subsoil compaction is a widely known phenomenon, especially in Europe where 32% and 18% of the subsoils are, respectively, highly and moderately vulnerable to subsoil compaction (Akker et al. 2003). With increasing use of conventional agricultural vehicles, these numbers continue to increase if preventative actions are not taken. Subsoil compaction is difficult to measure, as the soil is not easily accessed. Due to ploughing, topsoil compaction is alleviated. Subsoil compaction, however, is more persistent, even where shrinkage, swelling and annual deep freezing is occurring (Akker et al. 2003), and it may even metamorphose into a permanent condition. This is especially true where subsoil compaction has affected the sediments below 40 cm into the ground. Consequently, it has transformed into a great concern in agriculture (Mossadeghi-Björklund et al. 2016). In the two vertical models, Cross-Section 1 and Cross-Section 2, the

scenarios M1, M2, and M3 were simulated to evaluate the effect that subsoil compaction has during various scenarios. Subsoil compaction appeared to affect the removal efficiency of the tile drain in the two cross-sections. During all of the scenarios, the tile drain in Cross-Section 2 was substantially more efficient than the tile drain in Cross-Section 1 (see Table 5-11). The decreased hydraulic conductivity in the compacted areas in Cross-Section 1 lead to the flow moving at a slower rate both vertically and horizontally, which appeared to have had a great influence on the dynamic of the model. An interesting aspect is that between the three scenarios, the tile drain had the lowest removal efficiency in both models during M2, which indicates that the removal efficiency also depends on the pattern of precipitation, and that the higher the incoming flux, the higher the removal is. When calculating the difference between the cross-sections in the three scenarios, the removal efficiency increased the most in M3 from Cross-Section 1 to Cross-Section 2. However, the difference was greater between the models in M2 than in M1, even though the removal efficiency was higher during M1 in both models.

6.3 *The positive sides of compaction*

Compaction might not merely have negative effects on soils and crop yields. Bouwman and Arts (2000) studied how compaction affects crop yields and soil biota and concluded that a moderate degree of compaction (approximately 4.5 t load) provides the highest crop yield due to an improved root-soil contact. Soils that have not been compacted might appear too loose and the contact between roots and soil particles is inhibited as a result. At high rates of compaction (between 8.5 and 14.5 t load), however, roots aren't able to penetrate into the deeper soil layers and are, consequently, only able to utilize the upper 20 cm of the soil (Bouwman and Arts 2000). According to Mossadeghi-Björklund et al. (2016), a moderate degree of compaction might also lead to an increase in the frequency of preferential flow due to a decrease in near-saturated hydraulic conductivity. As a result, the size of the largest conducting pores increases.

6.4 *Preventative actions against compaction*

It appears that some degree of compaction is regarded as the optimal condition of the sediments as it might increase the frequency of preferential flow and provide prime living-conditions for crops. With conventional agricultural practices being conducted mainly mechanically, this allows farmers to adjust their current practices without having to eliminate

the use of vehicles, which would be unrealistic. As stated by Akker et al. (2003), the best way to prevent subsoil compaction is “to take care that soil stresses in the subsoil caused by wheel loads on the surface do not exceed the strength of that subsoil.” Suggestions to reduce compaction are many, and includes, for instance, operating with low-pressure tires, addition of organic matter, and using units that carry out several operations simultaneously (which reduces the number of wheel passes) (Hamza and Anderson 2005). Especially animal manure might act as a preventative agent against subsoil compaction as it prevents transmission of stresses towards subsoil deeper into the ground (Soane 1990), which was demonstrated when the incorporation of cattle manure significantly counteracted the effects that load and wetness has on bulk density and soil strength (Mosaddeghi et al. 2000). Regardless of the method that is chosen to defeat excessive compaction, the use of pedotransfer functions will aid researchers and, hence, farmers in the understanding of the physical properties of their agricultural soil and hopefully be beneficial when deciding in what direction to take the next step.

7 Conclusion

In this thesis, soil samples have been analysed for water retention characteristics and grain size distributions. The results from these analyses have been used in the quantification of variability of soil physical properties across the field plot through a geostatistical analysis and in the design of two vertical cross-sections that have been implemented to simulate the effect of different precipitation patterns and amounts, as well as the effect of both topsoil and subsoil compaction. A time-lapse ERT sequence has also been implemented to investigate the temporal changes of resistivity values in the soil matrix during a period of snowmelt and induced infiltration. All the data was collected from a field plot southeast in the Skuterud catchment in Ås.

The analyses of the soil samples and the infiltration tests indicate to what degree density and hydraulic conductivity depend on and affect one another. Based on these tests, it is evident that increasing densities leads to decreasing hydraulic conductivities, which was further supported by the geostatistical analysis of the parameters derived through the field and laboratory measurements. The geostatistical analyses of the soil physical properties indicate how they are connected and depend on one another. The density of the soil samples appears negatively correlated to porosity, hydraulic conductivity, air permeability, air capacity, saturated water content, and the van Genuchten parameter α , while positively correlated to the content of sand and the van Genuchten parameter n . To increase the understanding of how the density and the other mentioned parameters might vary due to vehicular activity, it would be beneficial to excavate additional soil samples from the tire tracks.

The resulting kriged map of the residual water content raises questions regarding the soil sample analyses, as some samples had an unrealistically high value compared to the other samples. The map portrays how there were two areas with very high values, while the remaining plot had very low values. It is possible that they represent anomalies in the data set, though they might also be faulty due to, for instance, an error in the water retention characteristics analysis. If this is the case, it raises the question regarding the authenticity of the other resulting values from the same analysis. The α values, for instance, appear to be too low compared to the range of values they ought to be within for the soil type silt loam.

The implementation of soil sample analyses in computer modelling in HYDRUS have been used to evaluate the effect that both topsoil and subsoil compaction has on the soil physical properties and the movement of water in the unsaturated zone. Previous research has suggested that topsoil compaction is related to ground pressure, while subsoil compaction is related to total axle load independently of ground pressure. Both of the cross-sections were designed based on this knowledge. The simulations of water flow demonstrated how topsoil compaction might affect the direction of flow, as compaction of the soil is concentrated directly beneath the tires of the vehicle, while compaction in general affects the velocity of flow. While topsoil compaction may be reversed through actions such as ploughing, subsoil compaction is generally more persistent. The simulations indicated how the degree of subsoil compaction might be alleviated in periods of high incoming flux. Hence, the complications with subsoil compaction are most excessive in periods of low incoming flux, which might lead to surface runoff. However, as long as the flux is less than the field capacity, the soil ought to be able to withstand it. The simulations also demonstrated how the drainage efficiency of the tile drains increased with increasing hydraulic conductivity and incoming flux.

There is still a need of verification of the computer models to examine whether the resulting flow of water during the three simulations are realistic. Field methods might include implementing wells and performing tracer tests, which can prove beneficial as the simulated data can be compared to the observed data. Based on the research that has been conducted as of yet, however, it appears that the models are somewhat realistic in their designs and that they are adequate in demonstrating how compaction affects the rate of water flow through a vertical cross-section in the soil matrix.

The time-lapse ERT sequence provided an insight into what is occurring during a period of snowmelt. Applying ERT in partially or completely frozen soil matrix' may be challenging, which was demonstrated in this study. For instance, problems with the equipment itself might have occurred, as there were times when the Syscal delivered error values during the RS check of the electrodes. This raises the issue of whether all of the measurements are faulty, which may be caused by a poor electrode-soil connection. It is also possible that the electrodes were spaced with too large intervals to achieve good resolution of the topsoil. Several of the resulting ERT images display opposite changes in values than what was

expected initially. It is true that during periods of very low temperatures, the resistivity values may increase due to increasing fluid viscosity. However, during periods of high rates of infiltration due to rapid snowmelt, the resistivity values were still increasing. Ice lenses, ice-filled pores, and basal ice layers on the soil surface may inhibit infiltration and the snowmelt may become runoff. If this were the case, it would be expected that the resistivity values remained constant. Hence, it does not explain why the resistivity values increased. If assuming that nothing was wrong with the equipment, a plausible theory might include preferential flow ways through macro-pores that generated large amounts of water rapidly, which resulted in low water contents by the time of the ERT measurements. Further analyses are needed to be able to support this theory or propose an alternate advocated suggestion. For instance, a salt tracer test might be performed to detect the preferential flow and transport paths, as has previously been done by Robert et al. (2012).

8 Bibliography

- Afshar, A., M. Abedi, G.-H. Norouzi and M.-A. Riahi (2015). "Geophysical investigation of underground water content zones using electrical resistivity tomography and ground penetrating radar: A case study in Hesarak-Karaj, Iran." *Engineering Geology* **196**: 183-193.
- Akker, J. J. H. V. d., J. Arvidsson and R. Horn (2003). "Introduction to the special issue on experiences with the impact and prevention of subsoil compaction in the European Union." *Soil & Tillage Research* **73**(1-2): 1-8.
- Appelo, C. A. J. and D. Postma (2010). *Geochemistry, groundwater and pollution*. CRC Press.
- Aronica, G. T. and L. G. Lanza (2005). "Drainage efficiency in urban areas: a case study." *Hydrological Processes* **19**: 1105-1119.
- Arvidsson, J. (2001). "Subsoil compaction caused by heavy sugarbeet harvesters in southern Sweden. I. Soil physical properties and crop yield in six field experiments." *Soil & Tillage Research* **60**: 67-78.
- Bechmann, M., M. Stenrød, A. Pengerud, H. A. Grønsten, J. Deelstra, H. O. Eggestad and M. Hauken (2014). Erosjon og tap av program for jord- og vannovervåkning i landbruket (JOVA) for 1992-2013. Bioforsk. **Vol. 9 Nr. 84**.
- Børresen, T. (2011). SOIL PHYSICS: Pore size distribution and pF-analysis: By use of ceramic plate, sandbox and air pycnometer. Department of Plant and Environmental Sciences, Norwegian University of Life Sciences: 6.
- Børresen, T. and L. E. Haugen (2003). JORDFYSIKK, ØVELSESKURS: JORD221: FELT- OG LABORATORIEØVELSER. Institutt for plante- og miljøvitenskap, Norges landbrukshøgskole: 34.
- Bouwman, L. A. and W. B. M. Arts (2000). "Effects of soil compaction on the relationship between nematodes, grass production and soil physical properties." *Applied Soil Ecology* **14**: 213-222.
- Davis, J. C. (1983). *Statistics and data analysis in Geology*. John Wiley & Sons.
- DecagonDevices(1). (2015). "MPS-2 DIELECTRIC WATER POTENTIAL." Retrieved 20. October, 2015, from <http://www.decagon.com/products/soils/water-potential/mps-2-water-potential-temperature/>.
- DecagonDevices(2). (2015). "5TM SOIL MOISTURE AND TEMPERATURE SENSOR." Retrieved 20. October, 2015, from <http://www.decagon.com/products/soils/volumetric-water-content-sensors/5tm-soil-moisture-and-temperature-sensor/>.
- Domenico, P. A. and F. W. Schwartz (1998). *Physical and Chemical Hydrogeology*. John Wiley & Sons, Inc.
- eKlima. (2016). "Årsrapport - Døgnverdier." Retrieved 17. march, 2016, from http://sharki.oslo.dnmi.no/portal/page?_pageid=73,39035,73_39049&_dad=portal&_schema=PORTAL.
- Flowers, M. D. and R. Lal (1998). "Axle load and tillage effects on soil physical properties and soybean grain yield on a mollic ochraqualf in northwestern Ohio." *Soil & Tillage Research* **48**: 21-35.
- French, H. and A. Binley (2004). "Snowmelt infiltration: monitoring temporal and spatial variability using time-lapse electrical resistivity." *Journal of Hydrogeology* **297**: 174-186.

- Ghanbarian-Alavijeh, B., A. Liaghat, G.-H. Huang and M. T. V. Genuchten (2010). "Estimation of the van Genuchten soil water retention properties from soil textural data." *Pedosphere* **20**(4): 456-465.
- Greipsland, I., H. Borch, A. Engebretsen, C. Farkas, H. O. Eggestad and T. Krogstad (2013). Test av modeller for næringsstoffavrenning på Skuterudfeltet. *Bioforsk.* **Vol. 8 Nr. 57**.
- Hamza, M. A. and W. K. Anderson (2002). "Improving soil physical fertility and crop yield on a clay soil in Western Australia." *Australian Journal of Agricultural Research* **53**: 615-620.
- Hamza, M. A. and W. K. Anderson (2005). "Soil compaction in cropping systems: A review of the nature, causes and possible solutions." *Soil & Tillage Research* **82**: 121-145.
- Hauken, M. (2015). "JOVA-programmet." Retrieved 10. february, 2016, from http://www.bioforsk.no/ikbViewer/page/prosjekt/hovedtema?p_dimension_id=18844&p_menu_id=18851&p_sub_id=18845&p_dim2=18846.
- He, H., M. F. Dyck, B. C. Si, T. Zhang, J. Lv and J. Wang (2015). "Soil freezing-thawing characteristics and snowmelt infiltration in Cryalfs of Alberta, Canada." *Geoderma Regional* **5**: 198-208.
- Hillel, D. (2004). *Introduction to Environmental Soil Physics*. Elsevier Academic Press.
- Kalantari, Z., S. W. Lyon, L. Folkesson, H. K. French, J. Stolte, P.-E. Jansson and M. Sassner (2013). "Quantifying the hydrological impact of simulated changes in land use on peak discharge in a small catchment." *Science of the Total Environment* **466-467**: 741-754.
- Kalantari, Z., S. W. Lyon, P. E. Jansson, J. Stolte, H. K. French, L. Folkesson and M. Sassner (2015). "Modeller subjectivity and calibration impacts on hydrological model applications: an event-based comparison for a road-adjacent catchment in south-east Norway." *Sci Total Environ* **502**: 315-329.
- Krogstad, T., P. Jørgensen, T. Sogn, T. Børresen and A. G. Kolnes (1991). Manual for kornfordelingsanalyse etter pipettemetoden. Ås-NLH, Institutt for jordfag. **6**: 41.
- Kværnø, S. H., L. E. Haugen and T. Børresen (2007). "Variability in topsoil texture and carbon content within soil map units and its implications in predicting soil water content for optimum workability." *Soil & Tillage Research* **95**: 332-347.
- Mosaddeghi, M. R., M. A. Hajabbasi, A. Hemmat and M. Afyuni (2000). "Soil compactibility as affected by soil moisture content and farmyard manure in central Iran." *Soil & Tillage Research* **55**: 87-97.
- Mossadeghi-Björklund, M., J. Arvidsson, T. Keller, J. Koestel, M. Lamande, M. Larsbo and N. Jarvis (2016). "Effects of subsoil compaction on hydraulic properties and preferential flow in Swedish clay soil." *Soil & Tillage Research* **156**: 91-98.
- Mouazen, A. M., K. Dumont, K. Maertens and H. Ramon (2003). "Two-dimensional prediction of spatial variation in topsoil compaction of a sandy loam field-based on measured horizontal force of compaction sensor, cutting depth and moisture content." *Soil & Tillage Research* **74**: 91-102.
- Mueller, B., M. Hauser, C. Iles, R. H. Rimi, F. W. Zwiers and H. Wan (2015). "Lengthening of the growing season in wheat and maize producing regions." *Weather and Climate Extremes* **9**: 47-56.
- Nemes, A. (2015). SOILSPACE - Project description, NIBIO: 10.
- Oliver, M. A. and R. Webster (2014). "A tutorial guide to geostatistics: Computing and modelling variograms and kriging." *Catena* **113**: 56-69.
- Olsen, P. A. (1998). *Measuring and modelling macropores and preferential flow in structured soils*. PhD, Agricultural University of Norway.

- Øygarden, L., L. M. Rød, M. Stenrød, J. Deelstra, H. O. Eggestad, M. Bechmann, O. M. Eklo and G. H. Ludvigsen (2010). JOVA rammeplan 2010-2015: Jord og Vannovervåking i landbruket- JOVA. Bioforsk.
- Remy, N., A. Boucher and J. Wu (2009). Applied Geostatistics with SGeMS: A user's guide. Cambridge.
- Reynolds, J. M. (2011). An Introduction to Applied and Environmental Geophysics. Wiley-Blackwell, John Wiley & Sons, Ltd.
- Riley, H. (1996). "Estimation of physical properties of cultivated soils in southeastern Norway from readily available soil information." Norwegian Journal of Agricultural Sciences **25**: 37.
- Robert, T., D. Caterina, J. Deceuster, O. Kaufmann and F. Nguyen (2012). "A salt tracer test monitored with surface ERT to detect preferential flow and transport paths in fractured/karstified limestones." Geophysics **77**(2): 55-67.
- Rygalska, M. (2015). Kornfordelingsanalyse etter pipetmetoden, NMBU.
- Samouëlian, A., I. Cousin, A. Tabbagh, A. Bruand and G. Richard (2005). "Electrical resistivity survey in soil science: a review." Soil & Tillage Research **83**: 173-193.
- Saripalli, K. P., R. J. Serne, P. D. Meyer and B. P. McGrail (2002). "Prediction of diffusion coefficients in porous media using tortuosity factors based on interfacial areas." GROUND WATER **40**(4): 346-352.
- Schwartz, F. W. and H. Zhang (2003). Fundamentals of Ground Water. John Wiley & Sons, Inc.
- Šejna, M., J. Šimůnek and M. T. v. Genuchten (2014). HYDRUS user manual: The HYDRUS software package for simulating the two- and three-dimensional movement of water, heat, and multiple solutes in variably-saturated porous media. PC-Progress: 307.
- Seki, K. (2007). "SWRC fit - a nonlinear fitting program with a water retention curve for soils having unimodal and bimodal pore structure." Hydrology and Earth System Sciences Discussions **4**: 407-437.
- senorge.no. (2016). "Snømengde i millimeter." Retrieved 12. May, 2016, from <http://www.senorge.no>.
- Silva, V. R. d., D. J. Reinert and J. M. Reichert (2000). "Soil Strength as affected by combine wheel traffic and two soil tillage systems." Ciencia Rural **30**: 795-801.
- Šimůnek, J., M. T. v. Genuchten and M. Šejna (2012). HYDRUS technical manual: The HYDRUS software package for simulating the two- and three-dimensional movement of water, heat, and multiple solutes in variably-saturated porous media. PC-Progress: 260.
- Smith, C. W., M. A. Johnston and S. A. Lorentz (2001). "The effect of soil compaction on the water retention characteristics of soils in forest plantations." South African Journal of Plant and Soil **18**(3): 87-97.
- Soane, B. D. (1990). "The role of organic matter in soil compactibility: A review of some practical aspects." Soil & Tillage Research **16**: 179-201.
- Soane, B. D. and C. v. Ouwkerk (1995). "Implications of soil compaction in crop production for the quality of the environment." Soil & Tillage Research **35**: 5-22.
- Sørbotten, L.-E. (2011). Jord- og vannovervåking i landbruket (JOVA): Feltrapporter fra programmet i 2009. Bioforsk. **Vol. 6 Nr. 38**.
- Stolte, J. (2016). Rough sketch of the Skuterud catchment including the location of tile drains.
- USDA (1993). Soil Survey Manual. Soil Conservation Services, USA: U.S. Department of Agriculture: 315.

Wösten, J. H. M., A. Lilly, A. Nemes and C. L. Bas (1999). "Development and use of a database of hydraulic properties of European soils." Geoderma **90**: 169-185.

Appendix

Appendix A: Quaternary map of the Ås-Ski area including the colour coding in Norwegian

Appendix B: Precipitation data given in millimetres per day in the HYDRUS simulations

Appendix C: Images and coordinates of the ERT measurements across the field plot

Appendix D: Spatial variability of grain size distributions and in-situ water retention characteristics

Additional results with the exact coordinates of each sample can be found in the attached excel-files:

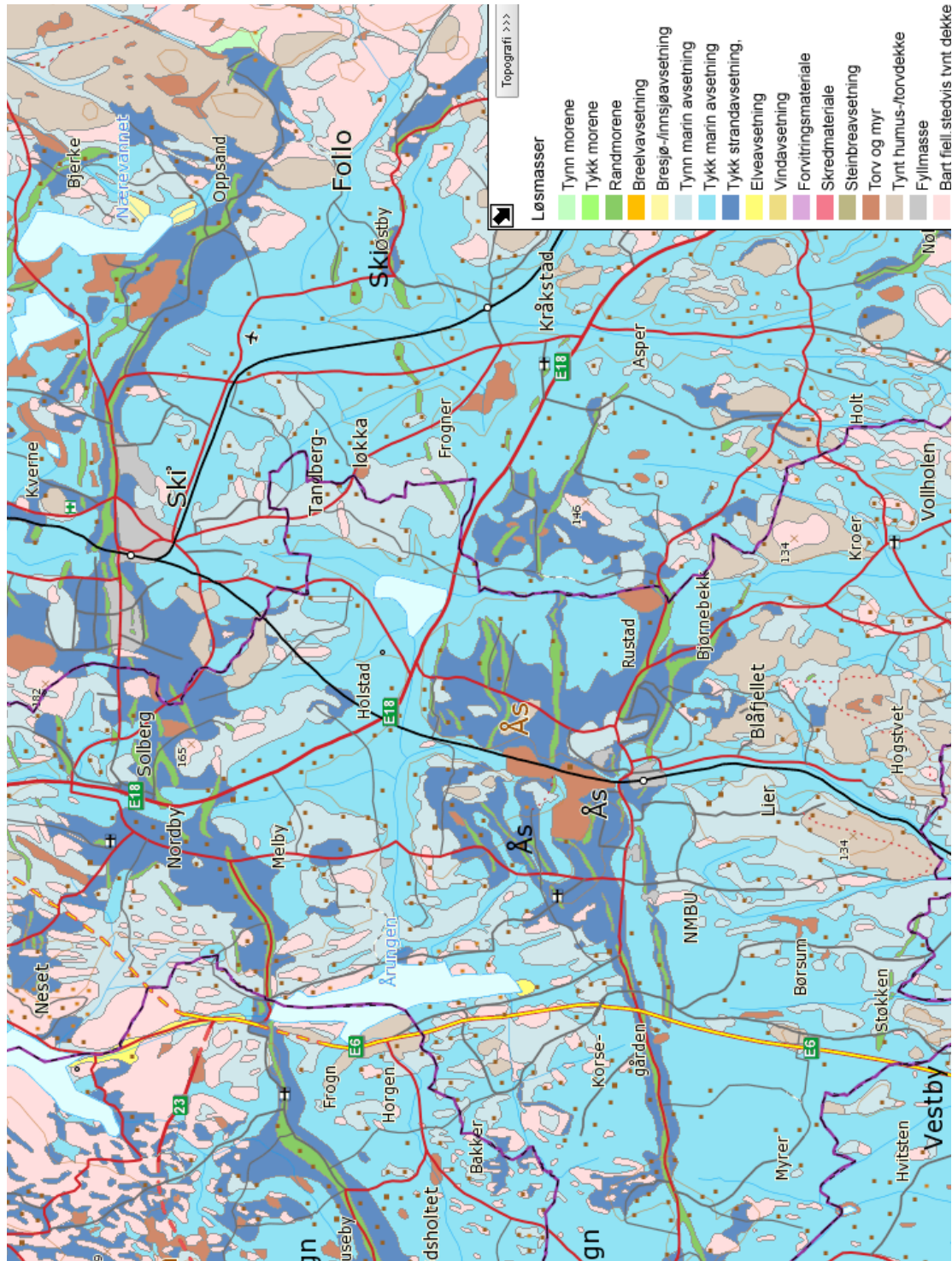
Fikse2016_pF_Skuterud.xls

Fikse2016_GSD_Skuterud.xls

Fikse2016_pF_InSitu_Skuterud.xls

Appendix A

Quaternary map of the Ås-Ski area including the colour coding in Norwegian



Appendix B

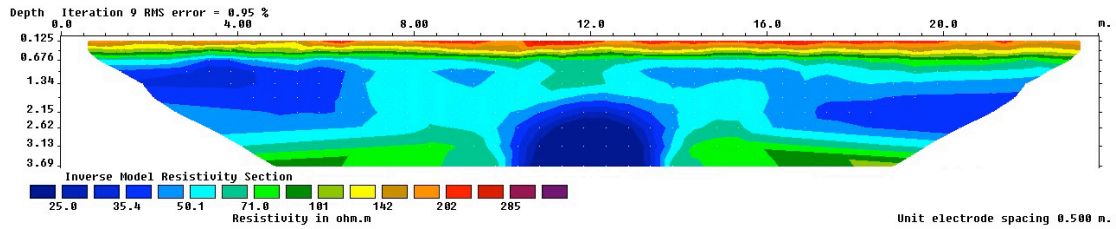
Precipitation data given in millimetres per day in the HYDRUS simulations

	M1	M2	M3	[Tracer] (mmol/m ³)	
1	10	10	10	1	Initial condition
2	0.7	0	7.3	0	Measured data
3	3.2	5	4.7	0	Measured data
4	15.3	0.2	16.8	0	Measured data
5	14.7	0.2	15.1	0	Measured data
6	1.3	0	0	0	Measured data
7	2.2	1.4	0	0	Measured data
8	11.2	0	0	0	Measured data
9	0.3	12.2	1	0	Measured data
10	0.5	3.6	9.8	0	Measured data
11	0.3	0	0.1	0	Measured data
12	0	0	11.2	0	Measured data
13	0	0	0	0	Measured data
14	0	0	2.8	0	Measured data
15	0	0.4	15.8	0	Measured data
16	0	7.4	0.6	0	Measured data
17	0	0.4	0.9	0	Measured data
18	0	0	1.1	0	Measured data
19	0	3	1.2	0	Measured data
20	0	0	0.7	0	Measured data
21	0	0	0.8	0	Measured data
22	0	0	2.3	0	Measured data
23	0	0	0.1	0	Measured data
24	0	0.4	0.2	0	Measured data
25	0	0	21.9	0	Measured data
26	0	1.3	3.4	0	Measured data
27	0	0	0.1	0	Measured data
28	0	0.5	0	0	Measured data
29	3.1	26.6	0.5	0	Measured data
30	1.4	0	0.1	0	Measured data
31	0.3	0	0	0	Measured data
32	3.4	0	0	0	Measured data

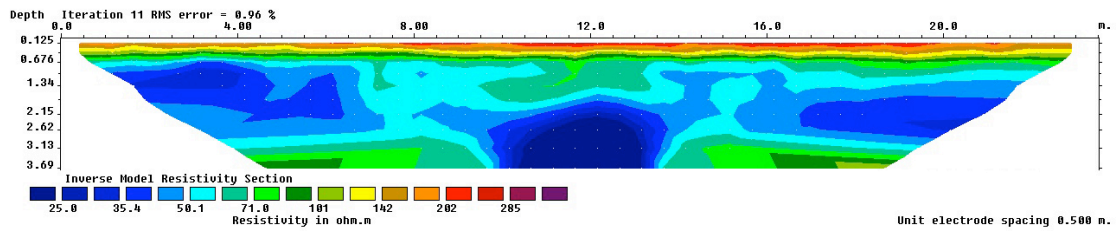
Appendix C

Images and coordinates of the ERT measurements across the field plot

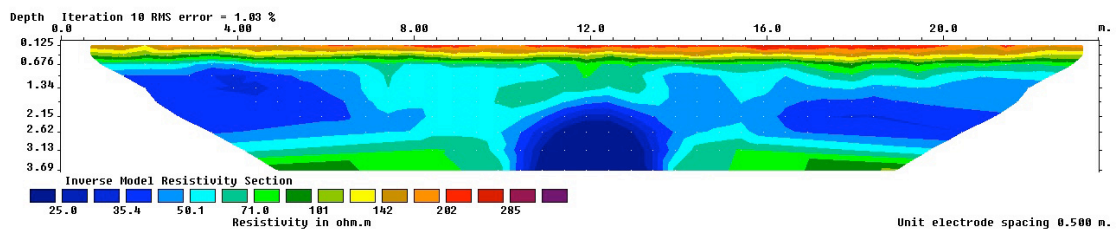
Line 1 X=0-23,5 Y=0



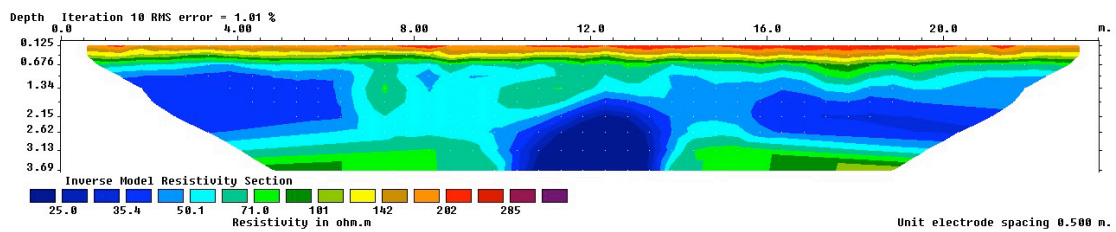
Line 2 X=0-23,5 Y=0,5



Line 3 X=0-23,5 Y=1

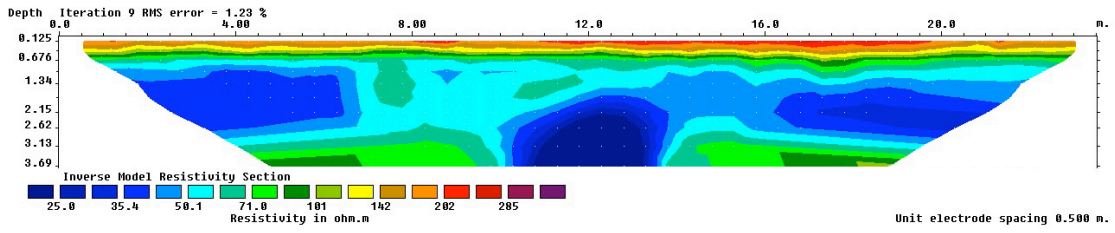


Line 4 X=0-23,5 Y=1,5

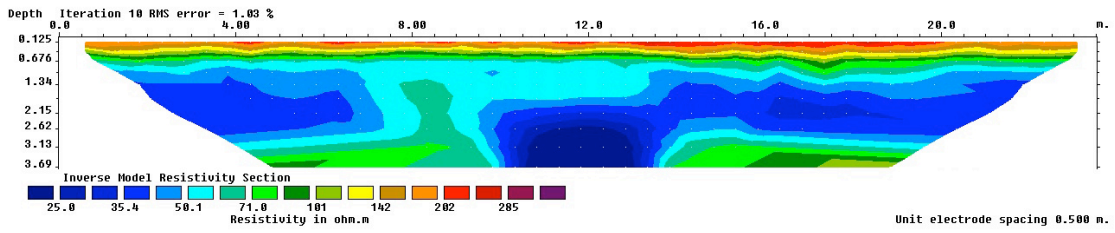


Appendix

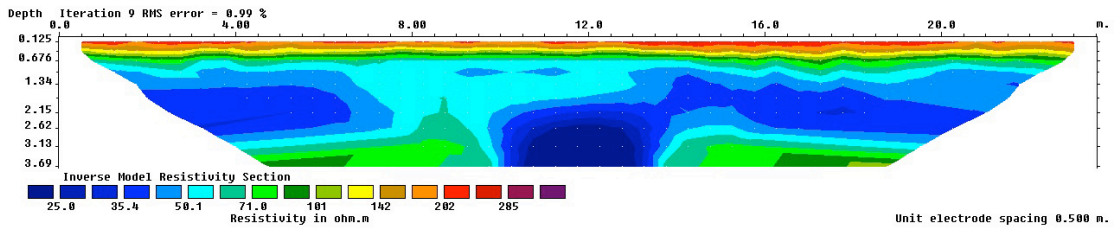
Line 5 X=0-23,5 Y=2



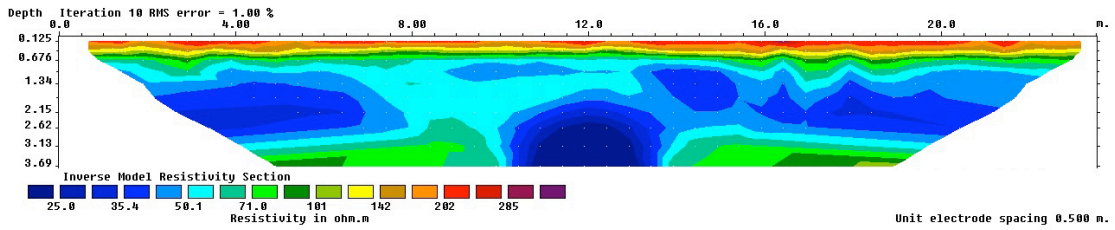
Line 6 X=0-23,5 Y=2,5



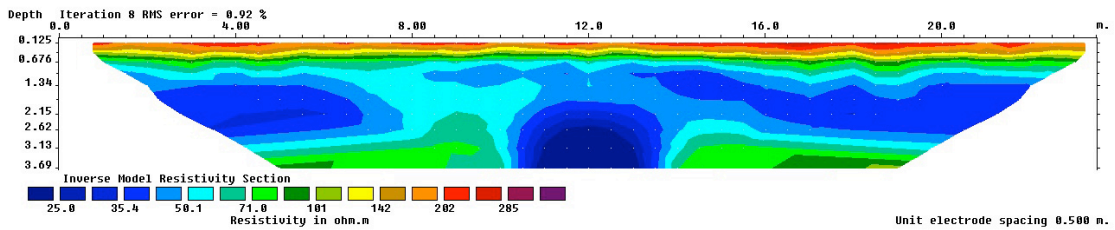
Line 7 X=0-23,5 Y=3



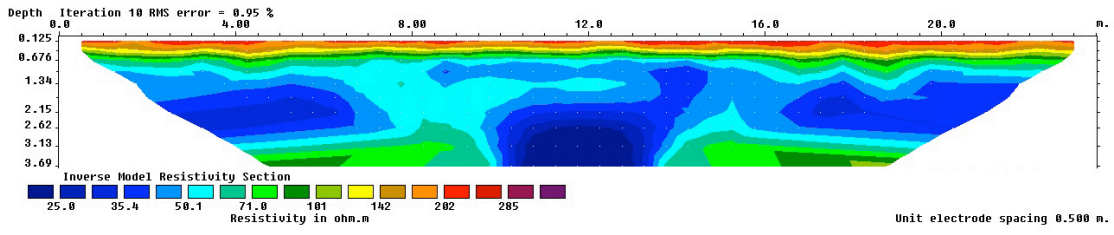
Line 8 X=0-23,5 Y=3,5



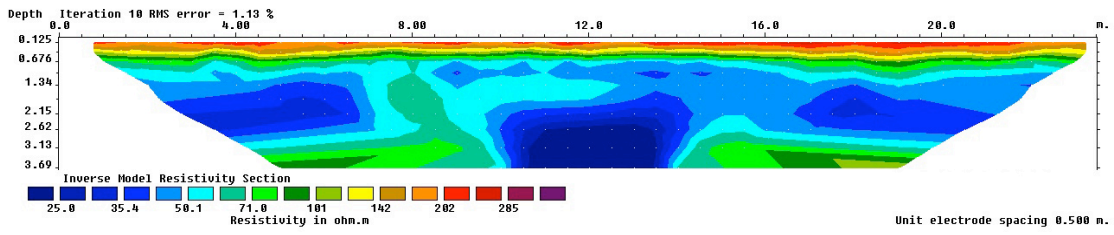
Line 9 X=0-23,5 Y=4



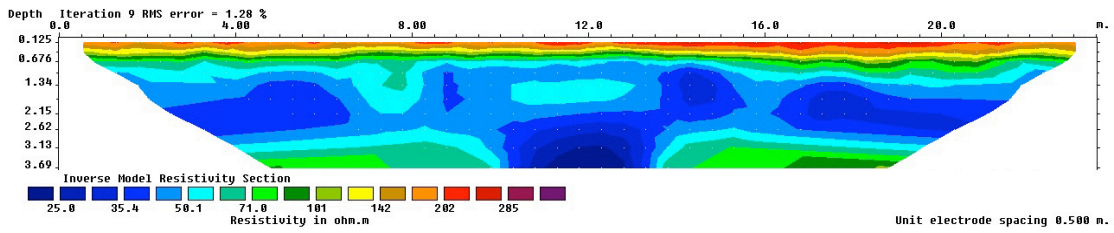
Line 10 X=0-23,5 Y=4,5



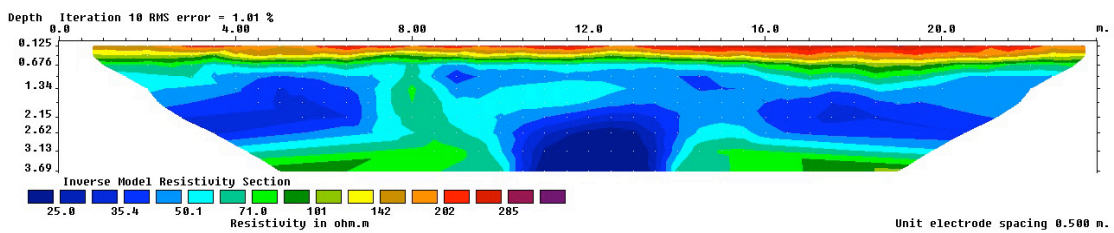
Line 11 X=0-23,5 Y=5



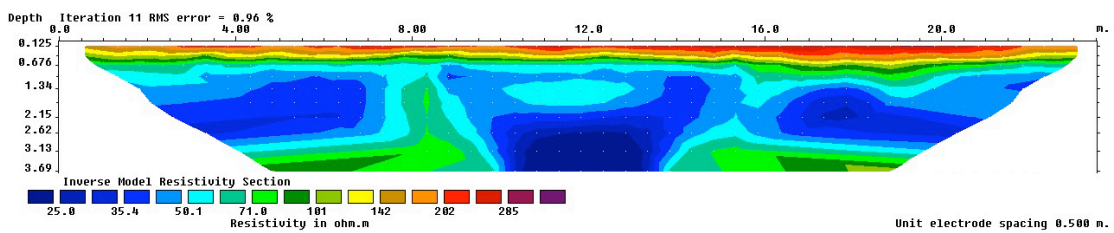
Line 12 X=0-23,5 Y=5,5



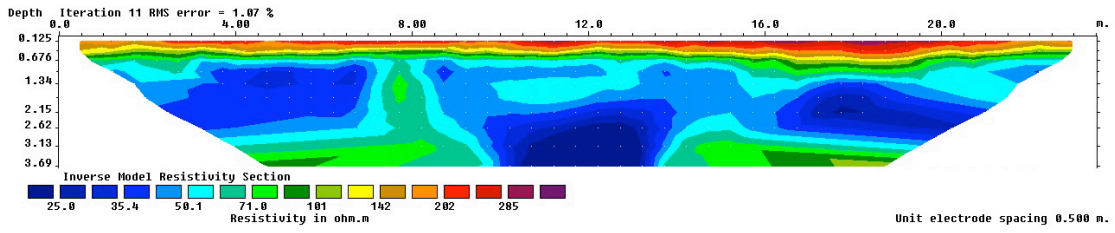
Line 13 X=0-23,5 Y=6



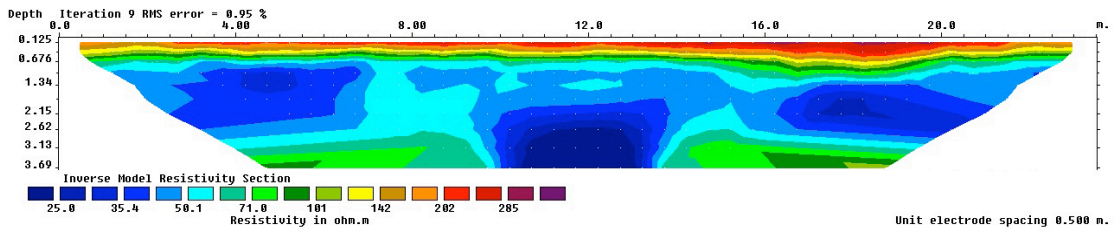
Line 14 X=0-23,5 Y=6,5



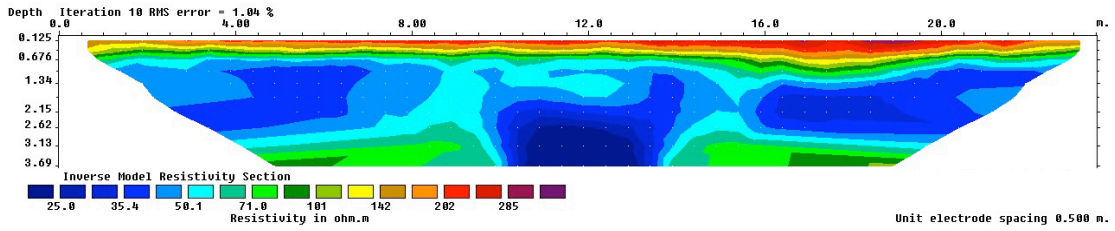
Line 15 $X=0-23,5$ $Y=7$



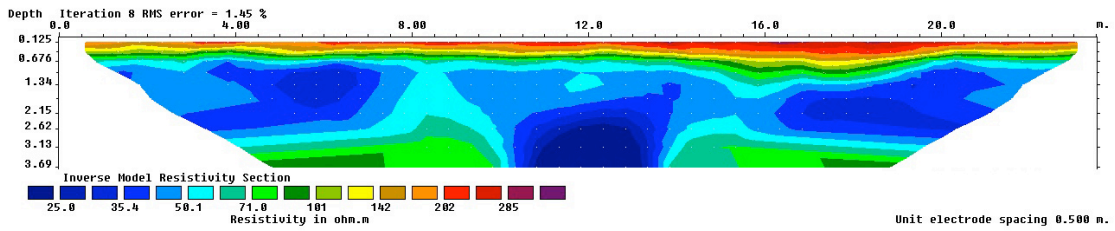
Line 16 $X=0-23,5$ $Y=7,5$



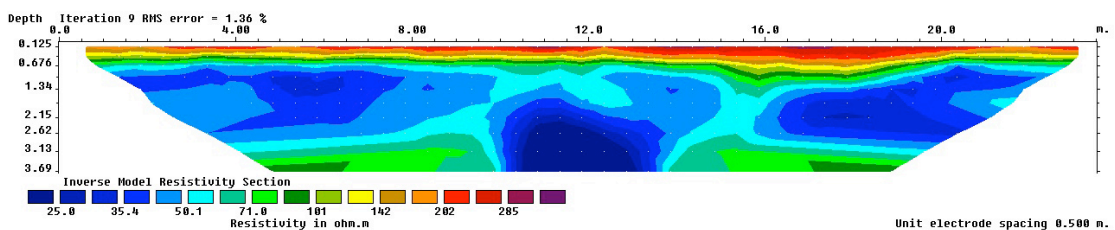
Line 17 $X=0-23,5$ $Y=8$



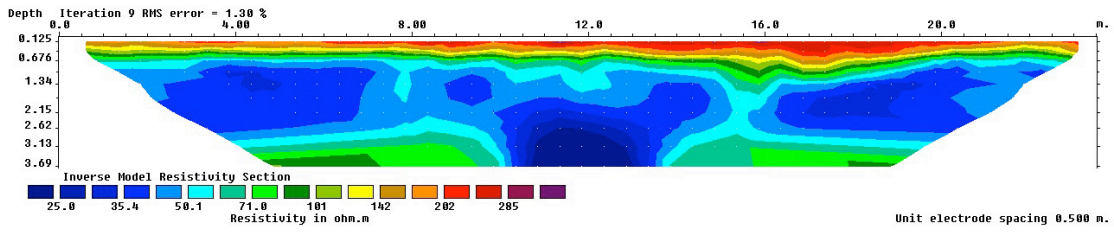
Line 18 $X=0-23,5$ $Y=8,5$



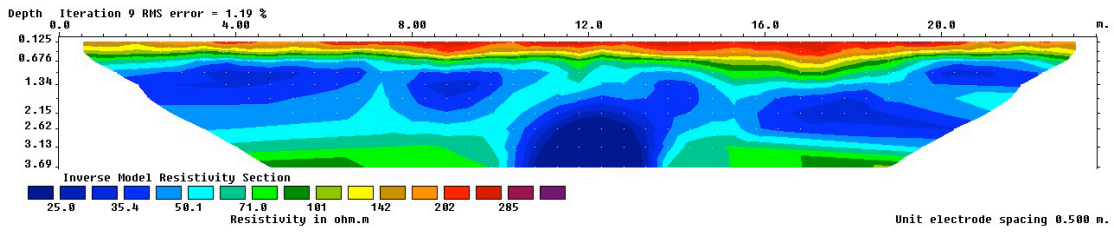
Line 19 $X=0-23,5$ $Y=9$



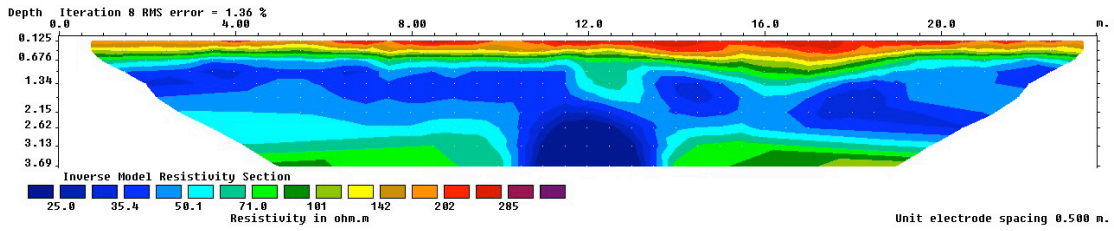
Line 20 X=0-23,5 Y=9,5



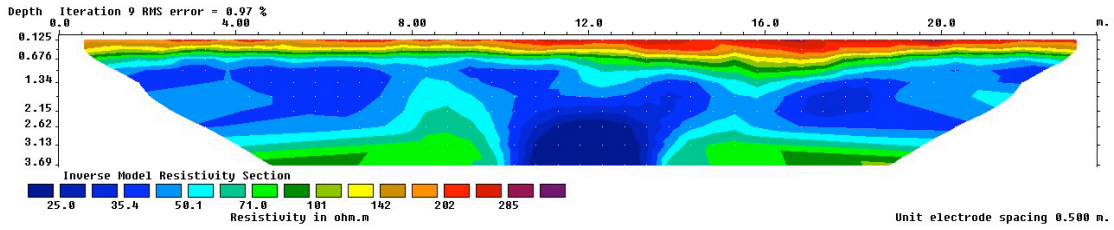
Line 21 X=0-23,5 Y=10



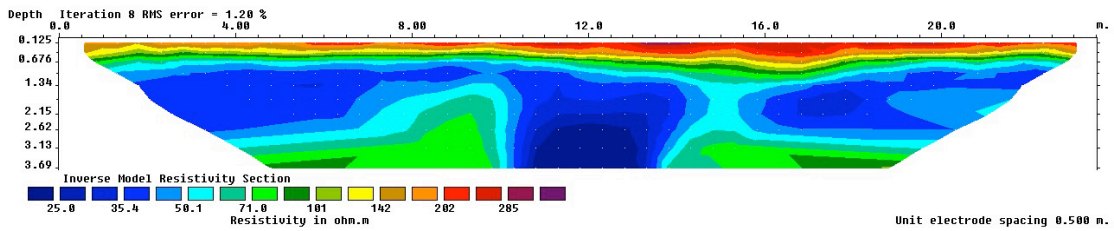
Line 22 X=0-23,5 Y=10,5



Line 23 X=0-23,5 Y=11



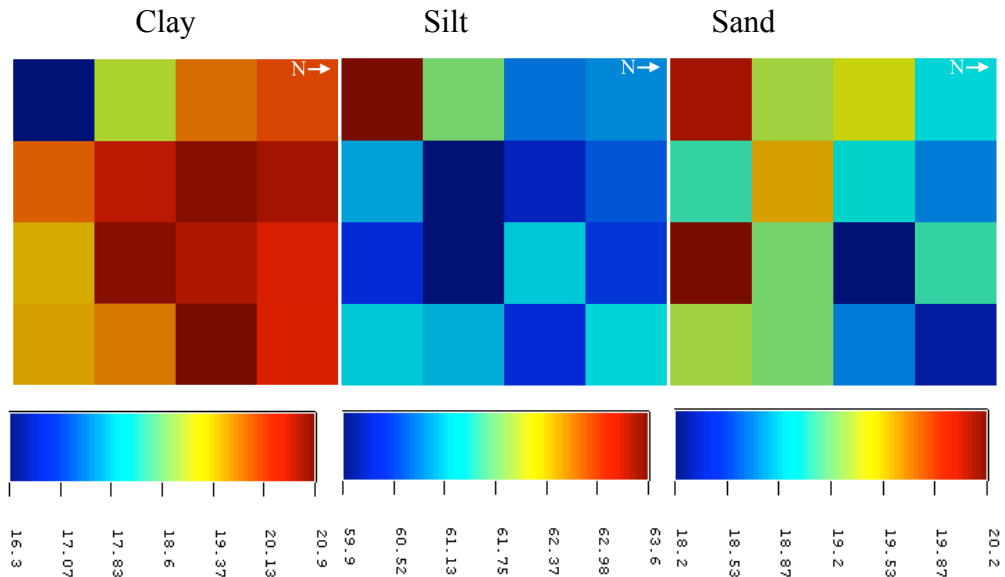
Line 24 X=0-23,5 Y=11,5



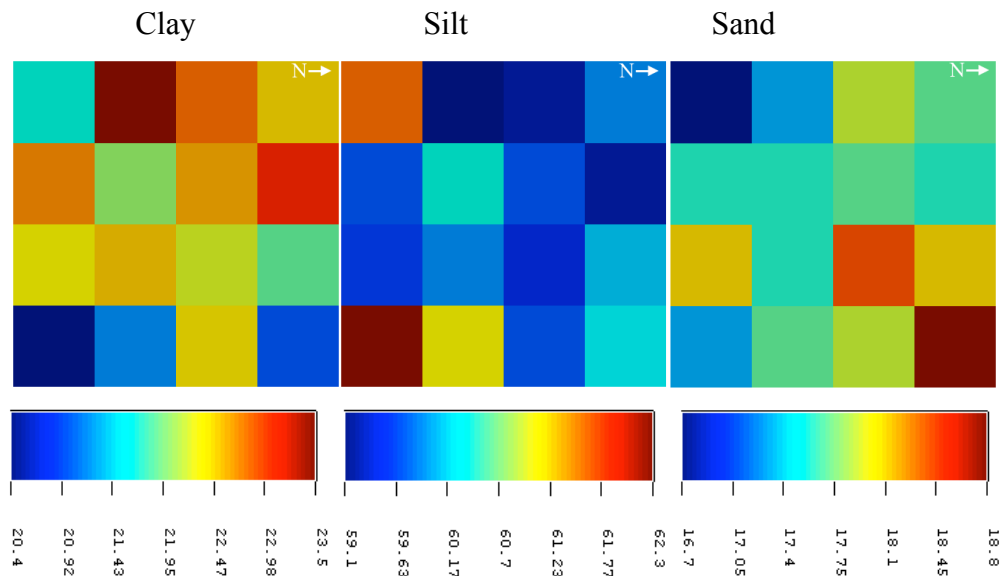
Appendix D

Spatial variability of grain size distributions with scale in %

Square 1 (X=3-6)

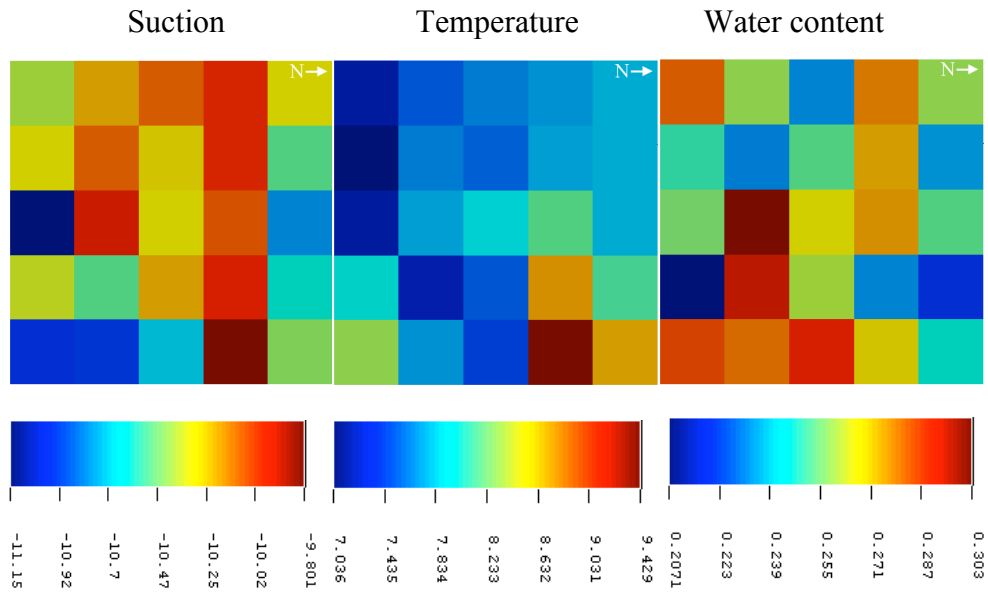


Square 2 (X=18-21)

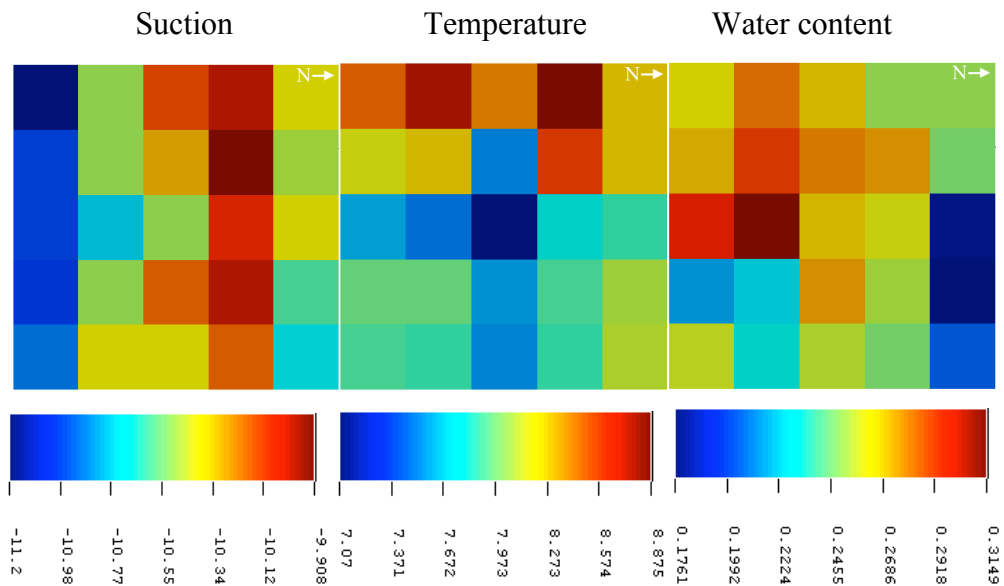


Spatial variability of in-situ measurements of retention characteristics where the scale for suction, temperature and water content are in kPa, °C, and m^3/m^3 , respectively

Square 1 (X=3-3.8)



Square 2 (X=18-18.8)





Norwegian University
of Life Sciences

Postboks 5003
NO-1432 Ås, Norway
+47 67 23 00 00
www.nmbu.no